https://doi.org/10.5194/egusphere-2026-3376
Preprint. Discussion started: 6 July 2026

Persistent decoupling weakens marine stratocumulus, with specific humidity inversions modulating microphysical and radiative responses

Jiaxing Zhang[1], Suying Yang[1], Chunsong Lu[1], Yiran Peng[2], Guan Ming[1,3], Jinbei Li[1]

[1] Key Laboratory for Aerosol-Cloud-Precipitation of China Meteorological Administration, Nanjing University of Information Science & Technology, Nanjing 210044, China
[2] Department of Earth System Science, Tsinghua University, Beijing 100084, China
[3]Jiande Meteorology Bureau of Hangzhou, Hangzhou 311600, China

Corresponding to: Suying Yang (ysy@nuist.edu.cn)

Abstract. Marine stratocumulus cloud (MSC) evolution is strongly influenced by boundary-layer coupling and turbulent mixing. However, under decoupled conditions, the impacts of specific humidity inversions (SHIs) on in-cloud mixing and microphysical evolution remain poorly constrained by in situ observations. Here, 12 persistently decoupled MSC cases from six flights during VOCALS-REx, POST, and ACE-ENA are analyzed to examine cloud microphysical, mixing, and radiative evolution with and without SHIs. Persistent decoupling generally suppresses MSC maintenance, reducing cloud thickness, liquid water content (LWC), mean droplet radius (r_m), and droplet spectral width. Without SHIs, dry air entrainment drives substantial upper-cloud LWC depletion under inhomogeneous mixing (IM)-dominated conditions, characterized by preferential evaporation of small droplets and super-adiabatic droplet formation, reducing cloud optical thickness (τ), albedo, and shortwave cloud radiative forcing. Conversely, when SHIs are present, moist air entrainment suppresses evaporative losses and modifies the microphysical consequences of IM by favoring collision–coalescence growth. Consequently, droplet spectra broaden toward larger sizes, super-adiabatic droplets form more readily, cloud dissipation is mitigated, and shortwave radiative forcing can be maintained or enhanced. Under sustained cloud-top moisture supply, SHIs can even support cloud maintenance or redevelopment. However, when droplet growth becomes sufficiently strong to promote precipitation-related cloud-water loss, cloud water and optical thickness may decline despite SHIs. Collectively, the observations suggest that MSCs under persistently decoupled boundary-layer conditions may follow distinct evolutionary pathways, including evaporative dissipation, moisture-driven cloud maintenance or redevelopment, and, in some cases, precipitation-related dissipation. These pathways have important implications for representing low-cloud shortwave radiative feedbacks in climate models.

1 Introduction

Marine stratocumulus cloud (MSC) exerts a substantial cooling effect on the Earth's radiation budget and represents one of the most important cloud regimes influencing the global climate system (Hartmann et al., 1992; Stephens and Greenwald, 1991; Wood, 2012; Yeom et al., 2021). MSC predominantly occurs within marine boundary layers under subtropical high-

https://doi.org/10.5194/egusphere-2026-3376
Preprint. Discussion started: 6 July 2026

pressure systems, particularly over the eastern ocean basins along the western coasts of major continents. MSC covers approximately 20% of the global ocean surface, with annual mean cloud fractions exceeding 60% in some regions(Hahn and Warren, 2007; Wood, 2012; Yeom et al., 2024). MSC strongly reflects incoming solar radiation (Chen et al., 2000) while exerting only a weak influence on outgoing longwave radiation, thereby producing a strong net cooling effect that substantially influences the Earth's radiation balance (Hartmann et al., 1992; Stephens and Greenwald, 1991). Cloud albedo is highly sensitive to the size and number distributions of cloud droplets (Twomey, 1974), such that even small variations in cloud fraction or cloud thickness can induce radiative forcing changes comparable in magnitude to those associated with increasing greenhouse gas concentrations (Hartmann and Short, 1980; Slingo, 1990). In addition, the microphysical and dynamical structures of MSC are highly sensitive to boundary-layer coupling state, turbulent mixing processes, and aerosol physicochemical properties (Desai et al., 2021; Duda et al., 1991; Glassmeier and Feingold, 2017; Prabhakaran et al., 2020; Yeom et al., 2021, 2024). Incomplete understanding of these interacting processes makes marine low clouds one of the major sources of uncertainty in climate sensitivity estimates (Cess et al., 1989; Mellado, 2017; Stevens, 2000; Wang et al., 2014; Yeom et al., 2021).

The maintenance of MSC primarily depends on turbulent mixing driven by cloud-top longwave radiative cooling and continuous moisture supply from the ocean surface. However, MSC exhibits pronounced horizontal and vertical inhomogeneity and is frequently accompanied by small-scale structures and drizzle processes, resulting in complex microphysical and radiative characteristics that remain difficult to parameterize accurately in global climate models (Brunke et al., 2022; Desai et al., 2021; Duda et al., 1991; Glassmeier and Feingold, 2017). The horizontal and vertical structures of MSC are closely linked to the thermodynamic structure of the boundary layer in which it is embedded (Albrecht et al., 1995; Bretherton et al., 2004, 2010; Wood and Hartmann, 2006). The stratocumulus-topped boundary layer (STBL), which covers extensive oceanic regions, is a key component of the climate system (Klein and Hartmann, 1993). Its structure is jointly regulated by surface sensible and latent heat fluxes, cloud-top longwave radiative cooling, evaporative cooling, and entrainment of warm and dry free-tropospheric air (Shin and Ha, 2009). Among these processes, convective instability induced by cloud-top longwave radiative cooling is the primary source of turbulence within the STBL, while surface buoyancy, wind shear, latent heat release, evaporative cooling, and cloud-top entrainment further enhance turbulent activity (Gerber et al., 2016; Lilly, 1968; Mellado, 2017; Stevens, 2002). Consequently, the thermodynamic structure and turbulent mixing characteristics of the STBL strongly depend on the degree of coupling between MSC and surface fluxes, particularly latent and sensible heat fluxes (Bretherton and Wyant, 1997; Xiao et al., 2011; Zheng et al., 2018b). Variations in coupling state directly modify the thermodynamic structure, moisture distribution, and cloud microphysical properties, thereby influencing MSC maintenance and radiative effects.

Decoupling refers to the separation of turbulent structures within the boundary layer arising from changes in buoyancy forcing and is particularly pronounced in cloud-topped boundary layer (CTBL), where it plays an important role in boundary-layer structure and MSC evolution (Bretherton and Wyant, 1997; Siebert et al., 2021). The decoupling process within the STBL is closely related to cloud radiative effects. During daytime, solar shortwave heating penetrates into the cloud layer and, together

https://doi.org/10.5194/egusphere-2026-3376
Preprint. Discussion started: 6 July 2026

with cloud-top longwave cooling, can destabilize the cloud layer and trigger separation between the cloud and sub-cloud layers (Considine, 1997; Driedonks and Duynkerke, 1989). Nicholls (1984) and Slingo et al. (1982) emphasized that such radiation-induced decoupling plays a key role in MSC dynamics. Once the boundary layer becomes decoupled, its mixing characteristics fundamentally change: moisture transport from the sea surface to the cloud layer is cut off, while entrained warm and dry air primarily heats and dries the cloud layer itself rather than mixing throughout the entire boundary layer, as occurs under coupled conditions (Driedonks and Duynkerke, 1989). Under these conditions, the boundary layer often exhibits pronounced vertical stratification, and the maintenance of in-cloud turbulence depends not only on cloud-top radiative cooling but also on wind shear and atmospheric stability (Chechin et al., 2023). Such dynamical changes directly influence cloud microphysical properties (Considine, 1997; Greenwald and Christopher, 2000). Because turbulent fluctuations play a critical role in aerosol activation (Prabhakaran et al., 2020), reduced turbulence intensity under decoupled conditions may suppress supersaturation fluctuations, thereby affecting activation processes and altering cloud droplet concentrations (Considine, 1997; Greenwald and Christopher, 2000). Previous studies, based on theoretical analyses and satellite observations, have demonstrated that decoupling substantially influences MSC dynamical structure and large-scale radiative effects (Bretherton and Wyant, 1997; Goren et al., 2018; Zheng et al., 2018a, b).

Turbulent entrainment and mixing are among the primary processes causing observed cloud droplet spectra to deviate from idealized adiabatic condensational growth theory (Yeom et al., 2017). In warm clouds, mixing between environmental dry air and cloudy air is commonly conceptualized as two limiting mechanisms: homogeneous mixing (HM) and inhomogeneous mixing (IM) (Baker et al., 1980; Warner, 1973; Yeom et al., 2017). Under HM conditions, all droplets experience similar evaporation rates, resulting in simultaneous decreases in droplet number concentration (N_c) and mean droplet size. In contrast, IM primarily reduces N_c while exerting relatively small influences on mean droplet size (Yeom et al., 2017). Previous studies have shown that the humidity of entrained air directly influences the evolution of mixing processes by regulating droplet evaporation rates and evaporation timescales. Lower environmental humidity accelerates droplet evaporation and favors IM, whereas higher humidity suppresses evaporation and allows turbulent mixing to develop more fully, thereby favoring HM (Gerber et al., 2008; Xu et al., 2022).

From a synoptic-scale perspective, the boundary layer exchanges heat, moisture, and momentum with the overlying free troposphere through turbulent processes. Consequently, free-tropospheric conditions strongly influence the evolution of boundary-layer clouds (Desai et al., 2021; Duda et al., 1991; Glassmeier and Feingold, 2017; Yeom et al., 2021, 2024). In recent years, increasing attention has been paid to the influence of free-tropospheric humidity structure on MSC evolution. Of particular relevance are specific humidity inversions (SHIs)—layers in which specific humidity increases with height near or above the cloud top, counter to the typical monotonic decrease expected in the free troposphere (Egerer et al., 2021; Nicholls and Leighton, 1986; Wood, 2012). Previous studies have shown that SHIs can weaken cloud-top radiative cooling by enhancing downward longwave radiation and suppress turbulent entrainment by reducing evaporative cooling, thereby influencing boundary-layer deepening and cloud lifetime (Dodson and Small Griswold, 2021; Eastman and Wood, 2018; Egerer et al., 2021). However, because SHIs in field observations frequently co-vary with inversion strength, large-scale

https://doi.org/10.5194/egusphere-2026-3376
Preprint. Discussion started: 6 July 2026

subsidence, and other environmental conditions, humidity-induced feedbacks are often difficult to isolate from broader thermodynamic background effects (Dodson and Small Griswold, 2021; Eastman and Wood, 2018). Egerer et al. (2021) revealed the impacts of SHIs on radiative and entrainment processes through detailed case observations, but comparable multi-case observational analyses remain limited.

Although previous studies have recognized the importance of both decoupling and cloud-top humidity structure, systematic observational evidence for common physical response mechanisms across different oceanic regions under persistently decoupled conditions remains limited. The present study analyzes 12 persistently decoupled MSC cases from the POST, VOCALS-REx, and ACE-ENA field campaigns, which sampled diverse oceanic regions including the southeastern Pacific, the California coast, and the North Atlantic. These campaigns provide a broad range of cloud-top humidity environments and high-resolution aircraft in situ observations capable of simultaneously characterizing cloud microphysical structure and turbulent mixing processes. Combined with radiative transfer calculations, these observations also enable diagnosis of shortwave cloud radiative forcing responses. Using these datasets, this study aims to identify common evolutionary characteristics of MSC microphysical structure, in-cloud mixing, and shortwave cloud radiative forcing under persistently decoupled conditions. Particular emphasis is placed on understanding how SHIs systematically modulate these evolutionary processes and thereby provide observational constraints for parameterizing low-cloud shortwave radiative feedback in climate models.

2 Data and methods

2.1 Data

This study is based on aircraft in situ observations from three field campaigns targeting MSC: VOCALS-REx, POST, and ACE-ENA. These campaigns were conducted over different oceanic regions and under distinct meteorological conditions, providing comprehensive measurements of boundary-layer thermodynamic structure, turbulent characteristics, and cloud microphysical properties. Together, these datasets provide a multi-case observational basis for investigating MSC evolution under persistently decoupled conditions and the modulating effects of SHIs.

The VOCALS-REx campaign (Wood et al., 2011) was conducted over the southeastern Pacific Ocean (10–30° S, 90° W to the Andes) during October and November 2008. This region, characterized by cold sea surface temperatures and large-scale subsidence, is one of the most representative marine stratocumulus regions worldwide. In this study, aircraft in situ observations collected by the CIRPAS Twin Otter aircraft are used. Flights were centered on Point Alpha (20° S, 72° W) and employed stacked horizontal flight legs at multiple levels. Individual flight legs were approximately 50–100 km in length and sampled below-cloud, in-cloud, and above-cloud layers at a true airspeed of approximately 60 $\mathrm{m\,s^{-1}}$. Turbulence and thermodynamic variables, including three-dimensional wind components, temperature, and humidity, were measured at 40 Hz using the AIMMS-20 probe system and corrected for aircraft motion using INS/GPS data. Cloud microphysical properties,

https://doi.org/10.5194/egusphere-2026-3376
Preprint. Discussion started: 6 July 2026

including droplet size distributions, N_c, and liquid water content (LWC), were measured at 1 Hz using the cloud and aerosol spectrometer (CAS) channel of the CAPS probe, which measures droplet diameters in the range of approximately 0.6–50 μm. The POST (Physics of Stratocumulus Top) campaign was conducted off the coast of Monterey Bay, California (35–39° N, 120–125° W), during July and August 2008, with the primary objective of investigating entrainment processes near MSC top and boundary-layer evolution(Gerber et al., 2010). Observations were performed using the CIRPAS Twin Otter aircraft, with approximately 17 research flights completed. Flight strategies primarily consisted of porpoising maneuvers vertically about the cloud-top region to detect fine-scale behavior, supplemented by horizontal flight legs below cloud and vertical profiles through the boundary layer. The aircraft true airspeed was approximately 55 m s^{-1}, and the vertical velocity during cloud-top penetrations was approximately 1.5 m s^{-1}. Turbulence and thermodynamic variables were measured using the University of California Irvine (UCI) 40 Hz turbulence probe package, including a gust probe for three-dimensional wind measurements, temperature, and humidity, with aircraft-motion corrections applied using INS/GPS data. Cloud microphysical properties, including droplet size distributions, N_c, and LWC, were measured at 1 Hz using the CAS channel of the CAPS probe, which measures droplet diameters in the range of approximately 0.5–50 μm.

The ACE-ENA (Aerosol and Cloud Experiments in the Eastern North Atlantic) campaign was supported by the Atmospheric Radiation Measurement (ARM) program of the U.S. Department of Energy and conducted over the northeastern Atlantic near the Azores during June–July 2017 (IOP1, summer) and January–February 2018 (IOP2, winter)(Wang et al., 2022). This region is influenced by multiple aerosol sources and is characterized by persistent and diverse subtropical marine boundary-layer low clouds. Observations were performed using the ARM Aerial Facility (AAF) Gulfstream-1 (G-1) aircraft. This study uses data collected during the first intensive operational period (21 June–20 July 2017). Aircraft operations were based at Lajes Airport on Terceira Island, approximately 90 km from the ENA ground site. Flight strategies included spiral ascents and descents together with stacked horizontal flight legs spanning below-cloud, in-cloud, cloud-top, and free-tropospheric layers over distances of several tens of kilometers. Flight directions included both along-wind and cross-wind sampling. Turbulence and thermodynamic variables, including three-dimensional wind components, temperature, humidity, and pressure, were measured at 20 Hz using the AIMMS-20 probe system. The horizontal wind speed accuracy was 0.50 m s^{-1}, and the temperature accuracy was 0.30 ℃. Aircraft-motion corrections were performed using INS/GPS data. Cloud microphysical properties, including droplet size distributions and N_c, were measured at 1 Hz using the Fast Cloud Droplet Probe (FCDP), which measures droplet diameters in the range of 1–50 μm with an approximate resolution of 3 μm. It should be noted that counting-efficiency corrections were not applied for the 1–10 μm size range.

To facilitate intercomparison among different campaigns and cases, all multi-instrument datasets were synchronized and aligned according to their timestamps, and data were resampled to common temporal resolutions when necessary. For analyses of vertical structure, altitude coordinates were normalized to reduce the influence of differences in cloud thickness and boundary-layer height among individual cases. Depending on the analysis objective, normalized heights were defined relative to either boundary-layer-top height or cloud thickness (see Sect. 2.2 for details).

https://doi.org/10.5194/egusphere-2026-3376
Preprint. Discussion started: 6 July 2026

2.2 Methods

To identify the common evolutionary characteristics of MSC under persistently decoupled conditions, this study adopts a multi-case composite analysis framework. Unlike studies emphasizing inter-case differences, the present work aims to extract common relationships among boundary-layer structure, turbulent characteristics, and cloud microphysical responses across multiple cases observed under different environmental conditions. It should be noted that cases without SHIs are primarily derived from VOCALS-REx observations, whereas cases with SHIs mainly originate from POST and ACE-ENA. This distribution reflects not only regional differences in cloud-top humidity structure but also possible influences of large-scale environmental conditions. To minimize the impact of regional differences among observational campaigns, the analysis focuses primarily on relative variations and vertical structural characteristics of physical variables rather than direct comparisons of their absolute magnitudes. To ensure inter-case comparability, consistent criteria for coupling state classification, boundary-layer height determination, and vertical normalization are applied throughout the analysis.

2.2.1 Determination of coupled and decoupled states

Following Jones et al. (2011), the coupled or decoupled state of the STBL is diagnosed based on the degree of turbulent mixing within the boundary layer. A coupled state corresponds to relatively uniform vertical distributions of conserved thermodynamic variables.

Specifically, the boundary layer is classified as coupled when both the liquid water potential temperature difference ($\Delta\theta_l$) and total water mixing ratio difference (Δq_t) between the top and bottom of the sub-cloud layer are sufficiently small:

$$\Delta\theta_l < 0.5\ \mathrm{K},\ \Delta q_t < 0.5\ \mathrm{g\ kg^{-1}}, \quad (1)$$

where $\Delta\theta_l$ and Δq_t denote the differences between the upper and lower portions of the sub-cloud layer. Cases in which at least one criterion is not satisfied are classified as decoupled, indicating insufficient turbulent mixing within the boundary layer.

2.2.2 Cloud identification, boundary-layer-top height, and vertical normalization

To ensure that the full vertical structure of the STBL was captured, only flight segments extending from the sub-cloud layer to above the cloud top were retained for analysis. Cloud samples were identified following Yeom et al. (2017) using thresholds of $LWC > 0.001\ \mathrm{g\ m^{-3}}$ and $N_c > 10\ \mathrm{cm^{-3}}$.

Following Dodson and Small Griswold (2021), the boundary-layer-top height (z_i) is defined as the altitude at which both the vertical gradient of water vapor mixing ratio satisfies $\partial q/\partial z \geq 0.1\ \mathrm{g\ kg^{-1}}$ and the potential temperature gradient satisfies $\partial\theta/\partial z \geq 0.2$ K.

To improve inter-case comparability of vertical structures, all variables are analyzed using normalized height coordinates. For analyses of boundary-layer structure, turbulent characteristics, and vertical cloud droplet spectral features, the normalized height is defined relative to the boundary-layer-top height as z/z_i, where z is the geometric altitude, such that the boundary-

https://doi.org/10.5194/egusphere-2026-3376
Preprint. Discussion started: 6 July 2026

layer top corresponds to a normalized height of 1. For in-cloud microphysical analyses, the normalized cloud-relative height is defined as $(z - z_{\mathrm{base}})/(z_{\mathrm{top}} - z_{\mathrm{base}})$, where z_{base} and z_{top} represent cloud-base and cloud-top heights, respectively. This normalization emphasizes relative in-cloud structural characteristics while minimizing the influence of differences in cloud thickness among cases.

2.2.3 Turbulence and thermodynamic parameters

Turbulent characteristics are quantified using statistical moments derived from high-frequency observations. Turbulent kinetic energy (TKE), representing turbulence intensity, is defined as:

$$TKE = \frac{1}{2}\left(\overline{u'^2} + \overline{v'^2} + \overline{w'^2}\right), \quad (2)$$

where u', v', and w' denote perturbations of the three-dimensional wind components. The third-order moment of vertical velocity (w'^3) is calculated from Reynolds decomposition averaged along the flight leg and is used to characterize the direction and intensity of turbulent transport (Dodson and Small Griswold, 2021; Nowak et al., 2021).

The lifting condensation level (Z_{LCL}) is used to characterize the thermodynamic structure of the sub-cloud layer, and its vertical variation reflects the degree of boundary-layer coupling:

$$Z_{\mathrm{LCL}} = \frac{T_{\mathrm{LCL}} - T}{-9.8} \times 1000, \quad (3)$$

where T_{LCL} is the temperature at Z_{LCL}, given by $T_{\mathrm{LCL}} = \left\{55 + \left[\frac{1}{T-55} - \frac{ln\frac{RH}{100}}{2840}\right]^{-1}\right\}$, with T being the absolute temperature and RH the relative humidity (Bolton, 1980).

To identify transition layers within the boundary layer, the stability parameter μ proposed by Yin and Albrecht (2000) is introduced:

$$\mu = -\frac{\partial\theta}{\partial p} + \frac{\varepsilon\theta}{1+\varepsilon q_{\mathrm{v}}}\frac{\partial q_{\mathrm{v}}}{\partial p}, \quad (4)$$

Where $\varepsilon = \frac{R_{\mathrm{V}}}{R_{\mathrm{d}}} - 1$, R_{V} and R_{d} are the gas constants for water vapor and dry air, respectively. A transition layer is considered to exist when μ exceeds 1.3 times the boundary-layer mean value.

Static stability is quantified using the Brunt–Väisälä frequency squared (Nb^2):

$$Nb^2 = \frac{g}{\theta_{\mathrm{V}}}\frac{\partial\theta_{\mathrm{V}}}{\partial z}, \quad (5)$$

where θ_{V} is virtual potential temperature and g is gravitational acceleration.

The horizontal wind shear rate (Sh^2) is defined as:

$$Sh^2 = \left(\frac{\partial u}{\partial z}\right)^2 + \left(\frac{\partial v}{\partial z}\right)^2, \quad (6)$$

https://doi.org/10.5194/egusphere-2026-3376
Preprint. Discussion started: 6 July 2026

where u and v are the horizontal wind components. Larger Nb^2 and Sh^2 values indicate stronger static stability and stronger wind-shear contributions to boundary-layer turbulence respectively. The transition-layer criterion and turbulence diagnostics follow Nowak et al. (2021).

2.2.4 Cloud microphysical properties and mixing diagnostics

Cloud microphysical parameters are calculated from cloud droplet size distributions measured by the CAS or FCDP probes. Derived variables include N_c, LWC, mean droplet radius (r_m), droplet spectral standard deviation (σ_m), and relative dispersion (d), where $d = \sigma_m / r_m$ characterizes the relative width of the droplet size distribution.

To quantify the intensity of collision–coalescence processes, the collision–coalescence threshold parameter (T_f) proposed by Desai et al. (2021) is introduced:

$$T_f = \frac{P}{P_0} = \left[\frac{\int_{r_t}^{\infty} r^6 n(r) dr}{\int_0^{\infty} r^6 n(r) dr}\right]\left[\frac{\int_{r_t}^{\infty} r^3 n(r) dr}{\int_0^{\infty} r^3 n(r) dr}\right], \quad (7)$$

where the autoconversion threshold radius is $r_t \approx 4.09 \times 10^{-4} \beta_{con}^{1/6} \frac{{N_c}^{1/6}}{LWC^{1/3}}$, with $\beta_{con} = 1.15 \times 10^{23}$ being an empirical coefficient. Larger T_f values indicate stronger collision–coalescence growth.

To quantify the degree of mixing homogeneity, the homogeneous mixing degree (ψ) is defined as:

$$\psi = \frac{\arctan\left(\frac{1-r^3/r_0^3}{1-N/N_0}\right)}{\pi/2}, \quad (8)$$

where $\psi = 1$ corresponds to ideal HM, in which entrained air mixes uniformly with cloudy air and all droplets experience similar evaporation fractions. Conversely, $\psi = 0$ corresponds to ideal IM, in which entrained air mixes only with part of the cloud volume, leading to complete evaporation of droplets within that portion. Negative ψ values indicate the presence of super-adiabatic droplets (Desai et al., 2021).

A mixing diagram is further introduced to characterize in-cloud turbulent entrainment and mixing mechanisms (Yeom et al., 2017). The mixing fraction α is defined as:

$$\alpha = \frac{LWC}{LWC_a} = \frac{N_c}{N_a}\frac{V}{V_a} = \frac{N_c}{N_a}\frac{{r_m}^3}{r_a^3}, \quad (9)$$

where LWC_a is the maximum LWC, N_a is the N_c corresponding to the LWC_a, and V_a and r_a denote the corresponding droplet volume and radius, respectively.

2.2.5 Radiative characterization

To evaluate the radiative impacts of persistent decoupling on MSC evolution, the Santa Barbara DISORT Atmospheric Radiative Transfer (SBDART) model (Ricchiazzi et al., 1998) is used to calculate cloud radiative effects for each case. SBDART is based on the plane-parallel atmosphere assumption and solves the radiative transfer equation using the discrete-ordinate method (DISORT). The shortwave spectral range is set to 0.25–4.0 μm, and the surface albedo is prescribed as ocean

https://doi.org/10.5194/egusphere-2026-3376
Preprint. Discussion started: 6 July 2026

type. Solar zenith angles corresponding to the actual observational periods are used as model input. Background atmospheric profiles are constructed from aircraft in situ observations. Within the boundary layer, observed temperature, pressure, and water vapor profiles are used directly, while the upper atmosphere is supplemented using a midlatitude standard atmosphere profile to produce a complete atmospheric structure extending from the surface to 100 km altitude.

Cloud radiative effects are characterized using cloud optical thickness (τ) and cloud effective radius (r_e), which serve as key inputs for the radiative transfer calculations.

Based on these calculations, the top-of-atmosphere shortwave cloud radiative forcing ($SW\ CRF_{\mathrm{TOA}}$) is defined as:

$$SW\ CRF_{\mathrm{TOA}} = -\left(F^{\uparrow}_{\mathrm{TOA,cld}} - F^{\uparrow}_{\mathrm{TOA,clr}}\right), \tag{10}$$

where $F^{\uparrow}_{\mathrm{TOA,cld}}$ and $F^{\uparrow}_{\mathrm{TOA,clr}}$ denote the upward shortwave radiative fluxes at the top of the atmosphere under cloudy and clear-sky conditions, respectively.

The planetary albedo (A) is defined as:

$$A = \frac{F^{\uparrow}_{\mathrm{TOA}}}{F^{\downarrow}_{\mathrm{TOA}}}, \tag{11}$$

where $F^{\uparrow}_{\mathrm{TOA}}$ is the upward shortwave radiative flux at the top of the atmosphere and $F^{\downarrow}_{\mathrm{TOA}}$ is the incoming shortwave radiative flux at the top of the atmosphere. To quantify the net influence of clouds on the reflectivity of the Earth–atmosphere system, the albedo difference (ΔA) is further defined as:

$$\Delta A = A_{\mathrm{cld}} - A_{\mathrm{clr}}, \tag{12}$$

where A_{cld} and A_{clr} represent the planetary albedo under cloudy and clear-sky conditions, respectively.

3 Results

3.1 Selection of decoupled boundary-layer cases and analysis of boundary-layer characteristics

Six representative research flights from the three observational datasets were selected for analysis and are hereafter referred to as V-RF06, V-RF09, V-RF15, P-RF04, A-0707, and A-0711. Each flight included two observational cases separated by approximately 1–2 h within the same flight, yielding a total of 12 analyzed cases. Because the large-scale environmental conditions varied only weakly within a single flight, the systematic evolution of cloud microphysical properties between the two cases can be used to characterize MSC responses under persistently decoupled conditions. Figure 1 presents the time–height flight trajectories and LWC distributions for all flights. Each analysis period (yellow shaded region) includes a complete vertical profile extending from near the sea surface, through the sub-cloud layer and the stratocumulus layer, and into the free atmosphere above the boundary-layer top, thereby providing comprehensive sampling for subsequent analyses of thermodynamic structure and cloud microphysical properties.

https://doi.org/10.5194/egusphere-2026-3376
Preprint. Discussion started: 6 July 2026

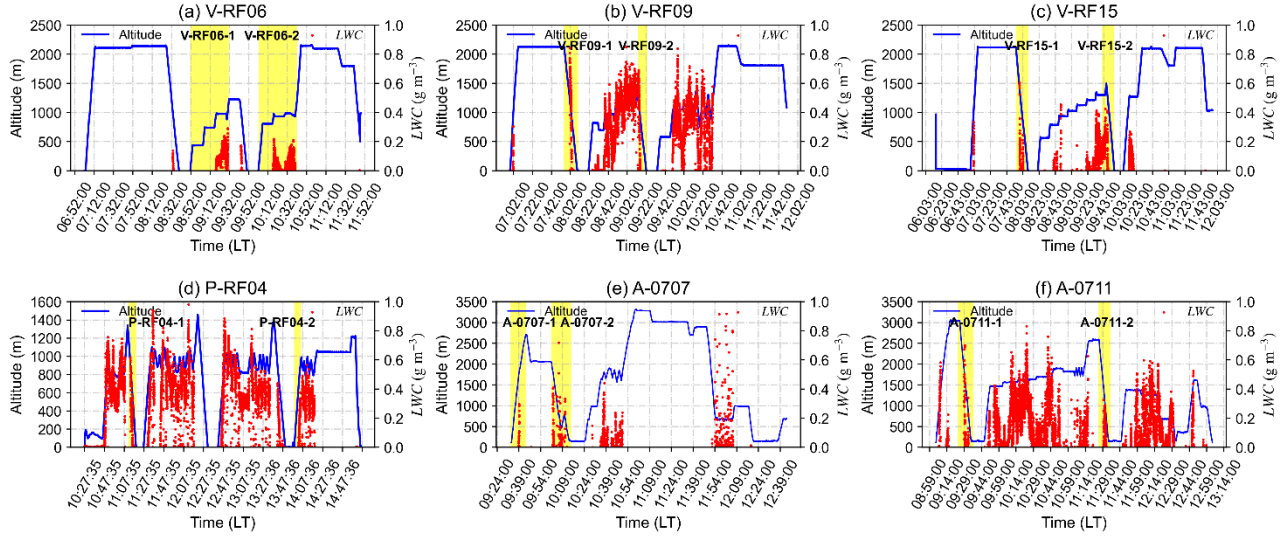

Figure 1: Time–height distribution of flight altitude (blue lines) and liquid water content (*LWC*, red dots) for all study cases. Yellow shaded areas indicate the analyzed periods.

Based on these complete cases, Fig. 2 further presents the vertical profiles of θ_l and q_t for all cases. All cases exhibit pronounced boundary-layer decoupling structures. Unlike coupled boundary layers, in which θ_l and q_t remain nearly constant from the surface to the top of the MSC layer, these cases display distinct vertical gradients of θ_l and q_t within the sub-cloud layer (Nowak et al., 2021). Such structures indicate suppressed turbulent mixing within the boundary layer, insufficient exchange between the surface layer and the cloud layer, and consequently weakened vertical transport processes.

The degree of decoupling in each case is further quantified in Table 1 using the differences in θ_l and q_t between the lower and upper portions of the sub-cloud layer, denoted as $\Delta\theta_l$ and Δq_t, respectively. According to the decoupling criteria described in Sect. 2.2.1, all 12 cases satisfy the decoupling conditions. The two V-RF06 cases ($\Delta\theta_l$= 1.28 K and 0.94 K) primarily exhibit thermodynamic stratification, whereas their Δq_t values remain below the threshold. In contrast, the remaining 10 cases exceed both threshold values simultaneously. Among them, A-0707 exhibits the strongest decoupling signatures, with $\Delta\theta_l$ values of 10.52 and 11.74 K and corresponding Δq_t values of 8.72 and 8.95 g kg^{-1}. Notably, both cases within each flight, despite being separated by 1–2 h, consistently satisfy the decoupling criteria, indicating that the decoupled state persisted throughout the observation periods. This persistent decoupling provides a stable dynamical background for subsequent analyses of MSC microphysical evolution.

Under this persistently decoupled background, the profiles in Fig. 2 reveal systematic differences in humidity structure near the cloud top among the analyzed cases. In the six cases from V-RF06, V-RF09, and V-RF15, no evident humidity inversion is observed near the cloud top, and q_t decreases rapidly with height near the boundary-layer top (Fig. 2a–f). In contrast, the six cases from P-RF04, A-0707, and A-0711 exhibit pronounced SHIs, characterized by q_t increasing or remaining nearly constant with height above the cloud top (Fig. 2g–l). In the cases with humidity inversions, the relative position between the inversion layer and the cloud top evolves with time. Specifically, in the two P-RF04 cases, the humidity inversion initially

https://doi.org/10.5194/egusphere-2026-3376
Preprint. Discussion started: 6 July 2026

remains directly attached to the cloud top (Fig. 2g) but later becomes separated from the cloud top by a finite distance (Fig. 2h). The two A-0707 cases exhibit a similar tendency, with the humidity inversion gradually detaching upward from the cloud top over time (Fig. 2i, j). In contrast, the SHIs in the two A-0711 cases remain continuously connected to the cloud top throughout the observations (Fig. 2k, l).

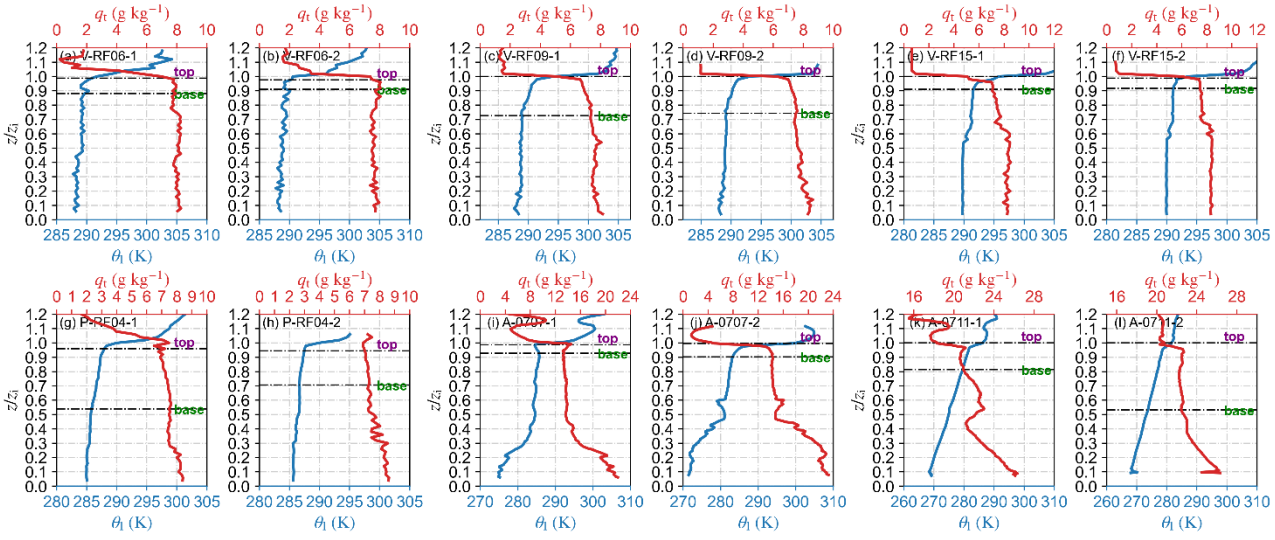

Figure 2: Vertical profiles of liquid water potential temperature (θ_l) and total water mixing ratio (q_t) for all cases. Dashed horizontal lines indicate cloud base and cloud top. The vertical coordinate is normalized by the boundary layer height (z/z_i).

Table 1. Flight Periods, Sub-cloud θ_l and q_t Gradients of the Studied Cases.

Date	Case	Local time (LT)	$\Delta\theta_l$ (K)	Δq_t (g kg^{-1})
2008.10.24	V-RF06-1	08:51:25-09:31:43	1.28	0.41
	V-RF06-2	10:01:55-10:41:53	0.94	0.14
2008.10.29	V-RF09-1	07:55:05-08:10:05	1.75	1.22
	V-RF09-2	09:12:55-09:23:25	2.37	1.40
2008.11.08	V-RF15-1	07:54:55-08:09:37	1.78	1.28
	V-RF15-2	09:39:55-09:55:45	1.04	0.80
2008.07.21	P-RF04-1	11:11:55-11:19:55	0.78	0.92
	P-RF04-2	13:58:56-14:05:56	1.06	1.29
2017.07.07	A-0707-1	09:34:33-09:43:53	10.52	8.72
	A-0707-2	10:01:13-10:14:53	11.74	8.95
2017.07.11	A-0711-1	09:23:00-09:36:00	9.56	3.21
	A-0711-2	11:25:00-11:35:00	5.76	3.91

Figure 3 shows that TKE exhibits large values near the surface and gradually decreases with height in all cases. Meanwhile, w'^3 is predominantly positive near the surface, indicating upward-developing turbulence generated by surface forcing. As

https://doi.org/10.5194/egusphere-2026-3376
Preprint. Discussion started: 6 July 2026

altitude increases, TKE progressively weakens, reflecting the gradual dissipation of turbulence during upward transport due to molecular viscosity and related damping processes. Near the cloud top, TKE again exhibits enhanced values that decrease downward with decreasing altitude. Combined with the negative values of w'^3, this feature suggests that the turbulence near cloud top is primarily generated by downward motions induced by cloud-top radiative cooling and weakens as it propagates downward. In the sub-cloud layer, however, TKE reaches a minimum and forms a distinct low-value region where w'^3 approaches zero, corresponding approximately to the decoupled layer. Although the altitude and thickness of the decoupled layer vary among cases, all cases consistently exhibit this characteristic pattern of turbulence generated from both the surface and cloud top but weakened within the middle layer, further confirming the persistent existence of decoupling during the observation periods.

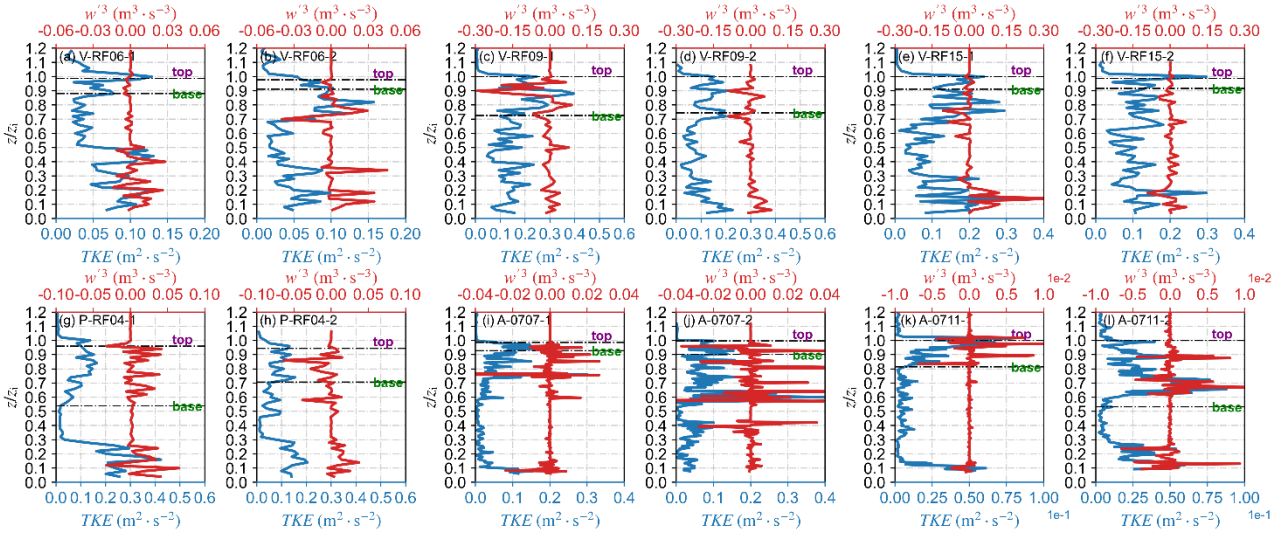

Figure 3. Same as Figure 2 but for turbulent kinetic energy (TKE) and third-order moment of vertical velocity (w'^3).

To more precisely determine the location of the transition layer, Fig. 4 presents the vertical distributions of Z_{LCL}, μ, Nb^2, and Sh^2 for the V-RF06 cases as representative examples.

Figure 4a shows that, in the V-RF06-1 case, Z_{LCL} varies only weakly with height within the normalized boundary-layer height range of 0.50–0.85 and gradually approaches a nearly constant value. This behavior indicates relatively dry air within this layer that is weakly influenced by upward turbulent transport from lower levels, representing a typical signature of boundary-layer decoupling. Within the same altitude range, μ exhibits pronounced fluctuations and locally reaches or slightly exceeds the threshold value of 0.014 (Fig. 4a), reflecting the presence of a thermodynamically stable transition layer beneath the cloud that suppresses turbulence. Nb^2 remains positive and nearly constant throughout most of the layer, including the cloud layer, while Sh^2 remains small near both the surface and within the cloud (Fig. 4b). These features indicate strong static stability in the sub-cloud layer, limiting the upward transport of surface-generated turbulence and thereby favoring decoupling. In Fig. 2a, θ_{l} and q_{t} also exhibit pronounced gradient changes near the normalized height of 0.5, while remaining relatively uniform

https://doi.org/10.5194/egusphere-2026-3376
Preprint. Discussion started: 6 July 2026

above and below this altitude, further indicating a distinct stratification boundary near this level. Combined with the vertical TKE structure shown in Fig. 3a, where surface-generated upward turbulence weakens substantially near the normalized height of 0.50 and cloud-top-driven downward turbulence weakens near 0.85, the transition layer in V-RF06-1 is identified as extending from 0.50 to 0.85.

Figure 4c shows that, in the V-RF06-2 case, Z_{LCL} increases slightly with height within the normalized altitude range of 0.37–0.50 before becoming nearly constant. Within the same layer, μ fluctuates and reaches or slightly exceeds the threshold value of 0.015 (Fig. 4c), suggesting the existence of a sub-cloud transition layer. Nb^2 remains positive and relatively constant over most of the profile, while Sh^2 remains weak near both the surface and within the cloud (Fig. 4d). These characteristics indicate strong static stability below the cloud and weak influence from surface-generated turbulence, thereby inhibiting efficient coupling between surface turbulence and the cloud layer. In combination with the distinct gradient changes of θ_{l} and q_{t} near the normalized height of approximately 0.35 in Fig. 2b, together with the weakening of upward and downward turbulence near normalized heights of 0.37 and 0.50, respectively, in Fig. 3b, the transition layer in V-RF06-2 is identified as extending from 0.37 to 0.50. The remaining 10 cases were analyzed using the same procedure, and the results are summarized in Fig. 5.

https://doi.org/10.5194/egusphere-2026-3376
Preprint. Discussion started: 6 July 2026

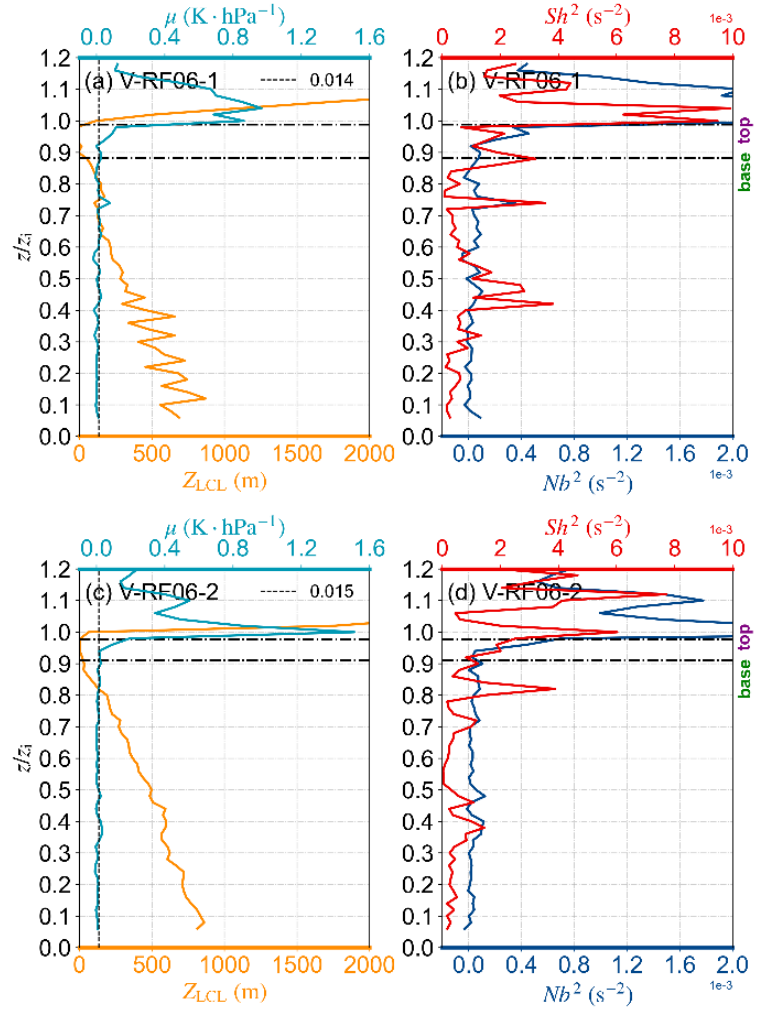

Figure 4. Vertical profiles of lifting condensation level (Z_{LCL}) and stability parameter (μ) in (a) and (c), and Brunt–Väisälä frequency squared (Nb^2) and horizontal wind shear rate (Sh^2) in (b) and (d) for the V-RF06 cases. Black dashed lines indicate cloud base and cloud top. The vertical coordinate is normalized by the boundary layer height (z/z_i).

Figure 5 demonstrates that, although the altitude and thickness of the transition layer differ among flights, all cases exhibit pronounced transition layers within the sub-cloud region. Combined with the quantitative results in Table 1, the distributions shown in Fig. 5 indicate that the two cases within each flight consistently maintain stable decoupled structures. This finding strongly confirms the persistence of decoupling throughout the observational periods. Such a stable and persistent decoupled background provides a consistent dynamical context for subsequent analyses.

https://doi.org/10.5194/egusphere-2026-3376
Preprint. Discussion started: 6 July 2026

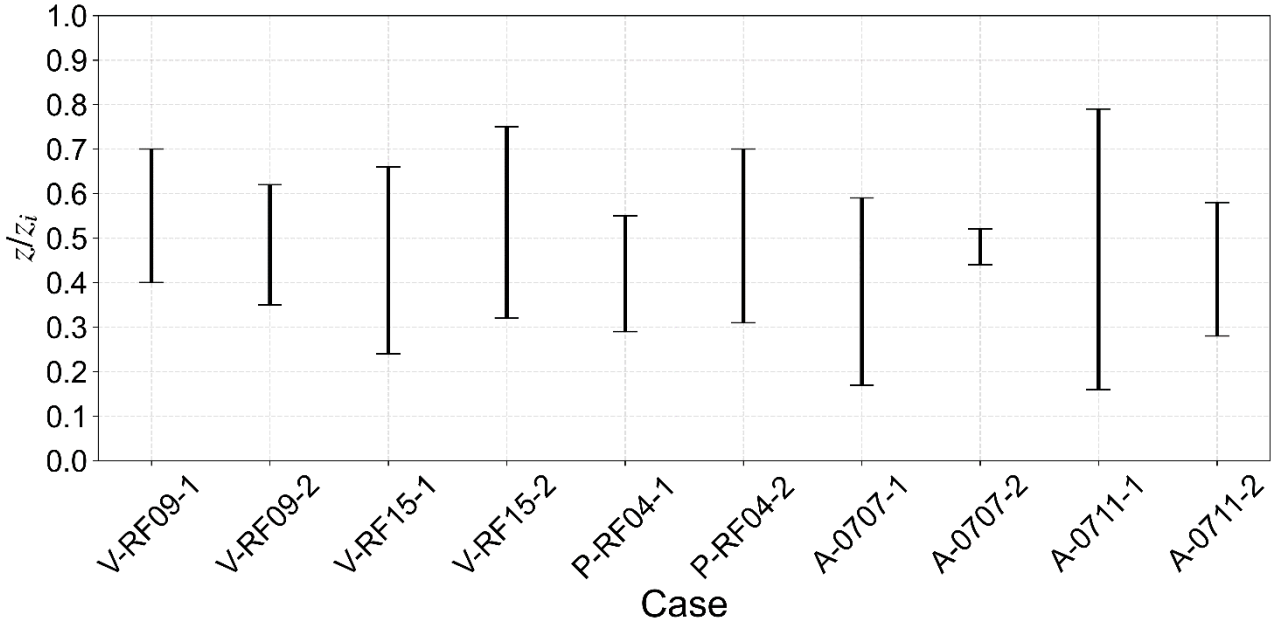

Figure 5. Normalized height ranges of the transition layers for all cases. The vertical coordinate is normalized by the boundary layer height (z/z_i).

3.2 Impacts of persistent decoupling on cloud microphysical properties

Section 3.1 demonstrated that all observed cases exhibited pronounced boundary-layer decoupling characteristics, and that the decoupled state persisted over time during each flight. Among them, the six cases observed during the V-RF06, V-RF09, and V-RF15 flights showed no evident SHI, whereas the six cases observed during the P-RF04, A-0707, and A-0711 flights exhibited SHIs. Based on this classification, the following analysis further investigates the impacts of persistent decoupling on the evolution of in-cloud microphysical properties.

First, cloud droplet spectra for all cases are presented (Fig. 6). Combined with the statistical characteristics of the droplet spectra and cloud microphysical parameters summarized in Table 2, the evolutionary characteristics of cloud droplet size distributions and cloud structures under persistent decoupled conditions are analyzed.

Figures 6a–f show that, in the absence of SHI, persistent decoupling was generally accompanied by cloud thinning. For example, during the V-RF06 flight, the normalized cloud thickness (th_{norm}) decreased from 0.119 to 0.096. During the V-RF09 and V-RF15 flights, th_{norm} decreased from 0.271 and 0.089 to 0.251 and 0.071, respectively (Table 2). In contrast, cases with SHI exhibited different evolutionary behaviors (Fig. 6g–l). Both the A-0707 and A-0711 cases showed increases in th_{norm} as decoupling persisted. Specifically, during the A-0707 flight, th_{norm} increased from 0.059 to 0.095, while during the A-0711 flight it increased substantially from 0.194 to 0.467. In the P-RF04 cases, th_{norm} decreased from 0.420 to 0.238. According to the mission flight logs (NSF NCAR – Earth Observing Laboratory, 1995–present), the aircraft traversed a

https://doi.org/10.5194/egusphere-2026-3376
Preprint. Discussion started: 6 July 2026

pronounced precipitation region during the P-RF04 observations, which may have contributed to the reduction in relative cloud thickness within the boundary layer.

Comparison of the vertical distributions of T_f among the droplet spectra further shows that cases with SHI generally exhibited larger T_f values, suggesting more active collision–coalescence growth. This conclusion is further supported by the statistical results in Table 2. For cases with SHIs, the spectral peak radius (R_{peak}) generally increased as decoupling persisted, while the corresponding peak droplet number concentration (N_{peak}) decreased. For example, during the A-0707 observations, R_{peak} increased from approximately 6.17 μm to 6.50 μm, whereas the corresponding N_{peak} decreased from approximately 13.18 cm^{-3} μm^{-1} to 12.68 cm^{-3} μm^{-1}. During the A-0711 observations, the changes were even more pronounced: R_{peak} increased from 5.83 μm to 6.67 μm, while N_{peak} decreased substantially from approximately 4.42 cm^{-3} μm^{-1} to approximately 2.00 cm^{-3} μm^{-1}. These results indicate that moisture supplied by the SHI promoted saturation in the upper cloud region, broadened the droplet spectrum, and enhanced collision–coalescence growth. As small droplets were continuously consumed and merged into larger droplets, N_{peak} decreased and the spectrum shifted toward larger droplet sizes. In particular, the P-RF04 cases exhibited notably large T_f values, with R_{peak} of approximately 7.5 μm and relatively low N_c, indicating vigorous collision–coalescence growth that effectively promoted precipitation formation, ultimately resulting in a marked reduction in relative cloud thickness within the boundary layer.

By contrast, cases without SHIs generally exhibited smaller T_f values, which further decreased over time. Their droplet spectra were primarily dominated by condensational growth, with generally larger N_{peak}. For example, the N_{peak} values of the V-RF06-1 and V-RF09-1 cases reached approximately 67 cm^{-3} μm^{-1} and 82 cm^{-3} μm^{-1}, respectively, reflecting that small-scale condensational growth dominated these cases. However, despite the absence of a distinct humidity inversion near cloud top during the V-RF09 observations, the droplet spectra still exhibited relatively large R_{peak} values and broader spectral widths, which may have been related to enhanced in-cloud mixing and collision–coalescence efficiency associated with the relatively large TKE observed during this flight (Fig. 3c, d).

https://doi.org/10.5194/egusphere-2026-3376
Preprint. Discussion started: 6 July 2026

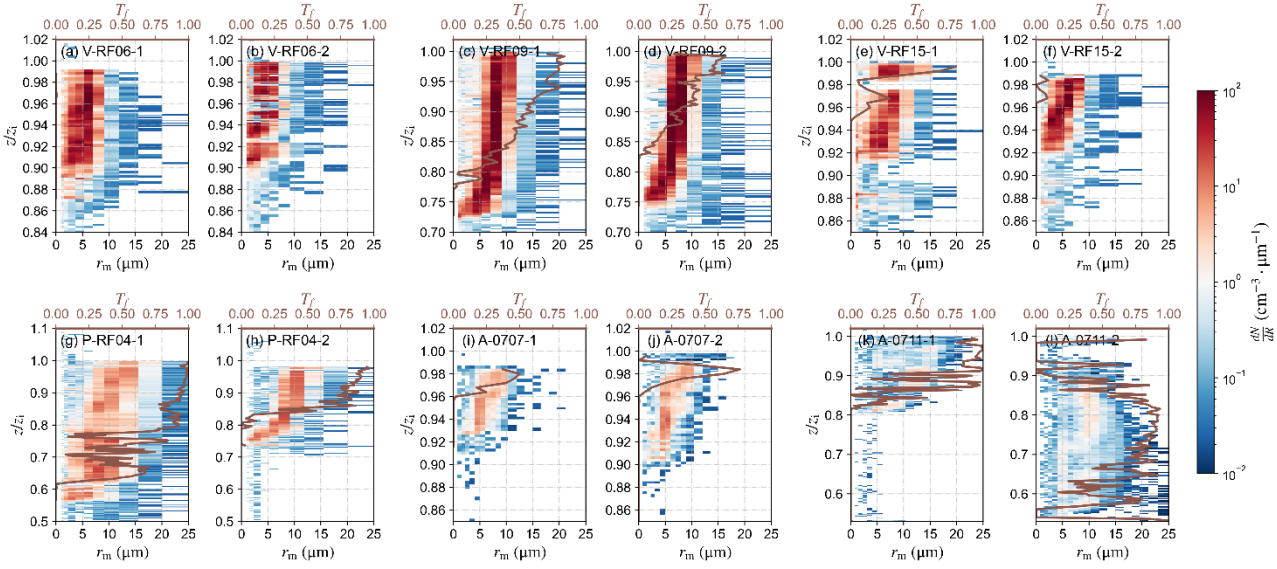

Figure 6. Cloud droplet size distributions for all cases. The vertical coordinate is normalized by the boundary layer height (z/z_i).

Table 2. Statistical characteristics of cloud droplet spectra and microphysical parameters for all cases.

Case	th_{norm}	N_{peak} (cm^{-3}μm^{-1})	R_{peak} (μm)	σ_c (μm)	LWC (g m^{-3})	N_c (cm^{-3})	r_m (μm)
V-RF06-1	0.119	67.16 ± 27.87	4.13 ± 1.58	23.42 ± 9.62	0.089 ± 0.080	176.4 ± 72.1	4.15 ± 1.15
V-RF06-2	0.096	31. 81 ± 33.12	2.83 ± 1.49	12.07 ± 11.93	0.054 ± 0.043	141.8 ± 74.0	3.70 ± 0.83
V-RF09-1	0.271	82.29 ± 21.91	7.15 ± 1.46	27.54 ± 7.60	0.481 ± 0.197	248.2 ± 48.4	7.29 ± 1.25
V-RF09-2	0.251	96.81 ± 30.02	6.30 ± 1.75	34.49 ± 11.53	0.410 ± 0.209	283.3 ± 66.1	6.40 ± 1.40
V-RF15-1	0.089	30.19 ± 17.26	6.25 ± 2.01	10.56 ± 6.07	0.133 ± 0.149	114.2 ± 59.7	6.45 ± 1.25
V-RF15-2	0.071	74.04 ± 24.41	5.69 ± 0.99	25.87 ± 8.27	0.099 ± 0.099	174.3 ± 70.3	4.80 ± 1.46
P-RF04-1	0.420	10.86 ± 7.13	7.47 ± 2.72	3.51 ± 2.25	0.252 ± 0.136	60.4 ± 20.6	8.73 ± 2.04
P-RF04-2	0.238	11.17 ± 5.73	7.58 ± 3.13	4.18 ± 2.29	0.157 ± 0.101	48.5 ± 11.0	8.23 ± 2.29
A-0707-1	0.059	13.18 ± 4.90	6.17 ± 2.21	4.44 ± 1.63	0.136 ± 0.089	88.8 ± 19.8	12.71 ± 2.64
A-0707-2	0.095	12.68 ± 8.06	6.50 ± 2.24	4.31 ± 2.86	0.115 ± 0.104	79.5 ± 35.4	12.22 ± 3.21
A-0711-1	0.194	4.42 ± 1.94	5.83 ± 3.06	1.21 ± 0.56	0.215 ± 0.180	31.0 ± 18.5	19.81 ± 4.15
A-0711-2	0.467	2.00 ± 2.71	6.67 ± 4.40	0.90 ± 0.96	0.141 ± 0.072	31.6 ± 11.9	17.79 ± 2.85

Note. All parameters except th_{norm} are presented as mean ± standard deviation.

To quantitatively characterize the magnitude and vertical variability of cloud microphysical evolution during persistent decoupling, Fig. 7 presents vertical profiles of the relative changes in microphysical variables between the later and earlier cases within the same flight. Here, the relative change is defined as the difference between the later and earlier cases normalized by the corresponding value in the earlier case, thereby representing the magnitude and vertical variability of microphysical evolution during persistent decoupling.

Figure 7 shows that during the V-RF06 observations, persistent decoupling was accompanied by substantial decreases in upper-cloud LWC, with reductions of approximately 50%–100%. N_c also decreased by approximately 50%, while r_m decreased by approximately 20%–60%. In contrast, reductions in LWC, N_c, and r_m in the lower cloud region were relatively small,

https://doi.org/10.5194/egusphere-2026-3376
Preprint. Discussion started: 6 July 2026

indicating comparatively stable conditions there. Regarding spectral-width parameters, σ_m remained nearly unchanged throughout the cloud layer, reflecting little change in the absolute spectral width. However, d increased in the upper cloud region, suggesting that although σ_m remained constant, the decrease in r_m caused the relative spectral width to broaden. Overall, the evolutionary characteristics of this flight reflect a typical cloud-top entrainment-mixing process: upper-cloud droplets were strongly influenced by entrainment mixing, leading to simultaneous decreases in LWC, N_c, and r_m due to droplet evaporation, whereas the lower cloud region, being farther from the entrainment layer, was less affected and remained relatively stable.

During the persistent decoupling observed in the V-RF09 flight, the relative change in LWC was negative throughout the cloud layer, with reductions of approximately 0%–50%, while r_m decreased by approximately 0%–30%. In contrast, N_c showed a slight overall increase within the cloud. Both σ_m and d decreased in the upper cloud region, indicating spectral narrowing that was not merely a proportional effect associated with r_m, but rather reflected a more concentrated droplet distribution with reduced size variability. Near cloud base, σ_m remained nearly unchanged while d increased. Combined with the decrease in r_m, this indicates that although the absolute spectral width remained unchanged, the reduction in r_m caused the spectrum to broaden in a relative sense. It should be noted that the overall increase in N_c does not imply enhanced droplet generation capability. Together with the pronounced decrease in th_{norm} during the persistent decoupling period, the increase in N_c mainly reflects the redistribution of droplets within a thinner cloud layer. Meanwhile, the continued decreases in LWC and r_m indicate that droplet growth remained suppressed and that the cloud layer was overall in a dissipating stage under sustained decoupled conditions.

The cloud microphysical evolution observed during the V-RF15 flight exhibited pronounced vertical stratification. LWC generally decreased by approximately 50%–100%, while r_m decreased by approximately 10%–50%. N_c increased in the upper cloud region but decreased by approximately 50% in the lower cloud region. Both σ_m and d decreased in the upper cloud region, suggesting spectral narrowing, whereas in the lower cloud region σ_m decreased while d remained relatively stable. Similar to V-RF09, the increase in upper-cloud N_c in V-RF15 was also primarily associated with vertical redistribution of droplets following cloud thinning. Combined with the substantial decreases in LWC and r_m, these results indicate that the cloud layer was undergoing dissipation, with suppressed droplet growth and a contracting cloud structure.

For the P-RF04 cases, which featured SHIs, Fig. 7 shows that the reduction in upper-cloud LWC (0%–50%) was smaller than that near cloud base (approximately 100%). N_c remained nearly unchanged in the upper cloud region, while reductions in the lower cloud region were mainly within 0%–50%. r_m slightly increased at some mid-cloud altitudes, consistent with active collision–coalescence growth there (Fig. 6g, h), whereas near cloud top r_m generally decreased by less than 20%, and decreased over time near cloud base. σ_m generally decreased throughout the cloud layer, while d remained relatively stable only near cloud base and decreased elsewhere, indicating overall spectral narrowing and a more concentrated droplet distribution with reduced size variability. It should be noted that raindrops were excluded from the present calculations; therefore, the decreases in r_m and σ_m mainly reflect the conversion of cloud droplets into raindrops during precipitation development.

https://doi.org/10.5194/egusphere-2026-3376
Preprint. Discussion started: 6 July 2026

During the A-0707 observations, except for slight increases in LWC at some upper-cloud altitudes, reductions in LWC across most of the cloud layer were mainly within 0%–50%, substantially smaller than those observed in cases without SHIs. N_c decreased markedly near cloud top, whereas at lower altitudes the relative changes became smaller and even showed slight increases in some regions. This behavior is consistent with the strongest collision–coalescence growth occurring near cloud top (Fig. 6i, j), where large droplets continuously consumed smaller droplets, while collision efficiency weakened in the middle and lower cloud regions, allowing reductions in N_c to diminish or even be offset by local vertical transport or condensational growth. r_m increased slightly only near cloud top, while decreasing elsewhere by approximately 0%–20%. Regarding spectral-width parameters, both r_m and σ_m increased slightly near cloud top while d remained unchanged, suggesting that additional moisture supplied by the SHI enlarged droplets and slightly broadened the absolute spectral width. However, because r_m and σ_m increased proportionally, the relative spectral width remained unchanged. Below cloud top, both r_m and σ_m decreased over time while d remained nearly constant, reflecting reduced moisture input away from the humidity inversion and narrowing of the absolute spectral width, while the simultaneous decrease in r_m maintained a nearly constant relative spectral width.

In the A-0711 cases, LWC exhibited vertically differentiated behavior, decreasing in the upper cloud region while increasing in the lower cloud region. N_c decreased by approximately 50%–100% near cloud top but generally increased elsewhere. r_m decreased slightly near cloud top while remaining relatively unchanged elsewhere. σ_m decreased near cloud top but increased near cloud base, remaining relatively constant elsewhere, indicating spectral narrowing near cloud top and slight spectral broadening near cloud base. The overall decrease in upper-cloud r_m may have been associated with weakened collision–coalescence growth over time, as T_f in the upper cloud region of A-0711-1 was substantially larger than that of A-0711-2 (Fig. 6k, l). The broadened droplet spectra near cloud base may have been related to increased T_f there. The evolutionary characteristics of this flight reflect a cloud redevelopment process under prolonged influence of the SHI: moisture supplied by the humidity inversion was gradually transported downward, leading to increases in LWC and N_c near cloud base and broadening of the droplet spectrum. Thus, the humidity inversion not only delayed cloud dissipation but also actively promoted the redevelopment of the cloud layer.

Overall, Figs. 6 and 7 indicate that persistent decoupling in cases without SHIs generally inhibits cloud maintenance and development, with the most prominent feature being substantial losses of microphysical quantities in the upper cloud region. These evolutionary characteristics suggest that persistent decoupling allows continued intrusion of cloud-top dry air, thereby enhancing droplet evaporation and causing simultaneous decreases in cloud water content and droplet size. By contrast, the lower cloud region, being farther from the entrainment layer, experiences smaller microphysical changes and remains relatively stable or only slightly weakens. The presence of humidity inversions substantially weakens the dissipative effects of persistent decoupling on the cloud layer. Continuous moisture supply from the humidity inversion markedly slows the decreases in LWC, r_m, and spectral-width parameters, and can even produce local increases at some altitudes. Regions directly in contact with the SHI are most sensitive, exhibiting increases in r_m, expansion or stabilization of σ_m, and enhanced collision–coalescence growth. In the middle and lower cloud regions, the influence gradually weakens. When the influence of the SHI is sufficiently

https://doi.org/10.5194/egusphere-2026-3376
Preprint. Discussion started: 6 July 2026

persistent and strong, as in A-0711, it can not only delay cloud dissipation but also trigger redevelopment of the cloud layer. It should also be noted that moisture supplied by the SHI may accelerate precipitation formation by enhancing collision–coalescence growth, as in P-RF04, thereby producing another form of cloud-water depletion dominated by precipitation removal.

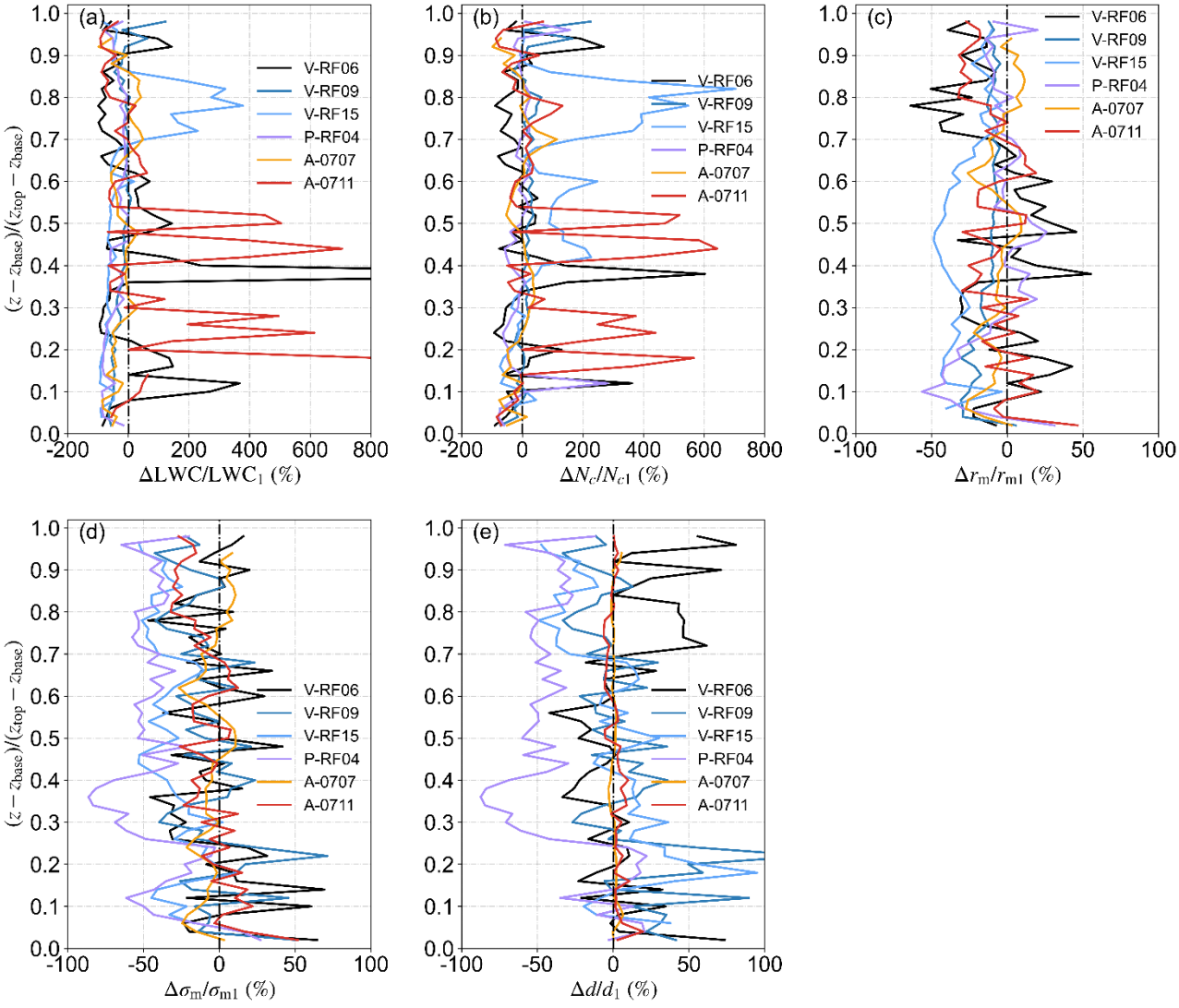

Figure 7. Vertical profiles of relative changes in cloud microphysical variables during persistent decoupling. Altitudes are normalized by the cloud layer thickness (cloud base = 0, cloud top = 1).

3.3 Impacts of persistent decoupling on in-cloud mixing characteristics

To reveal the vertical variability and temporal evolution of in-cloud mixing characteristics under persistently decoupled conditions, vertical profiles of ψ for different cases during each flight are presented in Fig. 8. Figure 8a shows that during the

https://doi.org/10.5194/egusphere-2026-3376
Preprint. Discussion started: 6 July 2026

V-RF06 observations, as decoupling persisted, ψ in the upper cloud region (defined as the region where ψ exhibited predominantly negative values) evolved from predominantly negative values to predominantly small positive values while still containing some negative values. In the lower cloud region, ψ remained positive and increased slightly over time. These results indicate that the upper cloud region maintained IM-dominated conditions accompanied by the formation of super-adiabatic droplets, while the degree of IM in the lower cloud region exhibited a slight decrease as decoupling persisted. During the V-RF09 observations, ψ in the upper cloud region remained predominantly negative in both cases, indicating persistent IM-dominated conditions accompanied by super-adiabatic droplets, whereas ψ in the lower cloud region remained generally positive and exhibited little systematic change over time (Fig. 8b), This behavior suggests that the influence of persistent decoupling on mixing characteristics was primarily confined to the upper cloud region during the V-RF09 observations. Figure 8c shows that during the V-RF15 observations, ψ in the upper cloud region evolved from small positive values to negative values, while ψ in the lower cloud region remained positive and increased slightly over time. This indicates that the upper cloud region evolved from IM toward more strongly IM-dominated conditions accompanied by super-adiabatic droplets, whereas IM in the lower cloud region weakened slightly over time. During the P-RF04 observations, negative ψ values persisted in the upper cloud region, whereas ψ in the lower cloud region remained positive and shifted toward larger values over time (Fig. 8d), consistent with persistent IM-dominated conditions with super-adiabatic droplets aloft and weakened IM in the lower cloud region. Figure 8e shows that during the A-0707 observations, ψ throughout most of the cloud layer, except near cloud base, evolved from small positive values to conditions containing localized negative values over time, suggesting a transition toward more strongly IM-dominated conditions accompanied by super-adiabatic droplets. Near cloud base, however, ψ remained positive and exhibited little change over time. Figure 8f shows that during the A-0711 observations, ψ remained generally positive throughout the cloud layer and increased over time, indicating that both cases remained IM-dominated while the degree of IM weakened as decoupling persisted.

Overall, negative ψ values frequently occurred near cloud top, indicating that IM remained the dominant mixing regime in the upper cloud region and was often accompanied by the formation of super-adiabatic droplets. In contrast, ψ in the lower cloud region generally remained positive and exhibited only small temporal variations during most flights. Except for P-RF04, which showed a pronounced increase in ψ over time, the remaining flights displayed only slight increases or little systematic change in lower-cloud ψ as decoupling persisted.

https://doi.org/10.5194/egusphere-2026-3376
Preprint. Discussion started: 6 July 2026

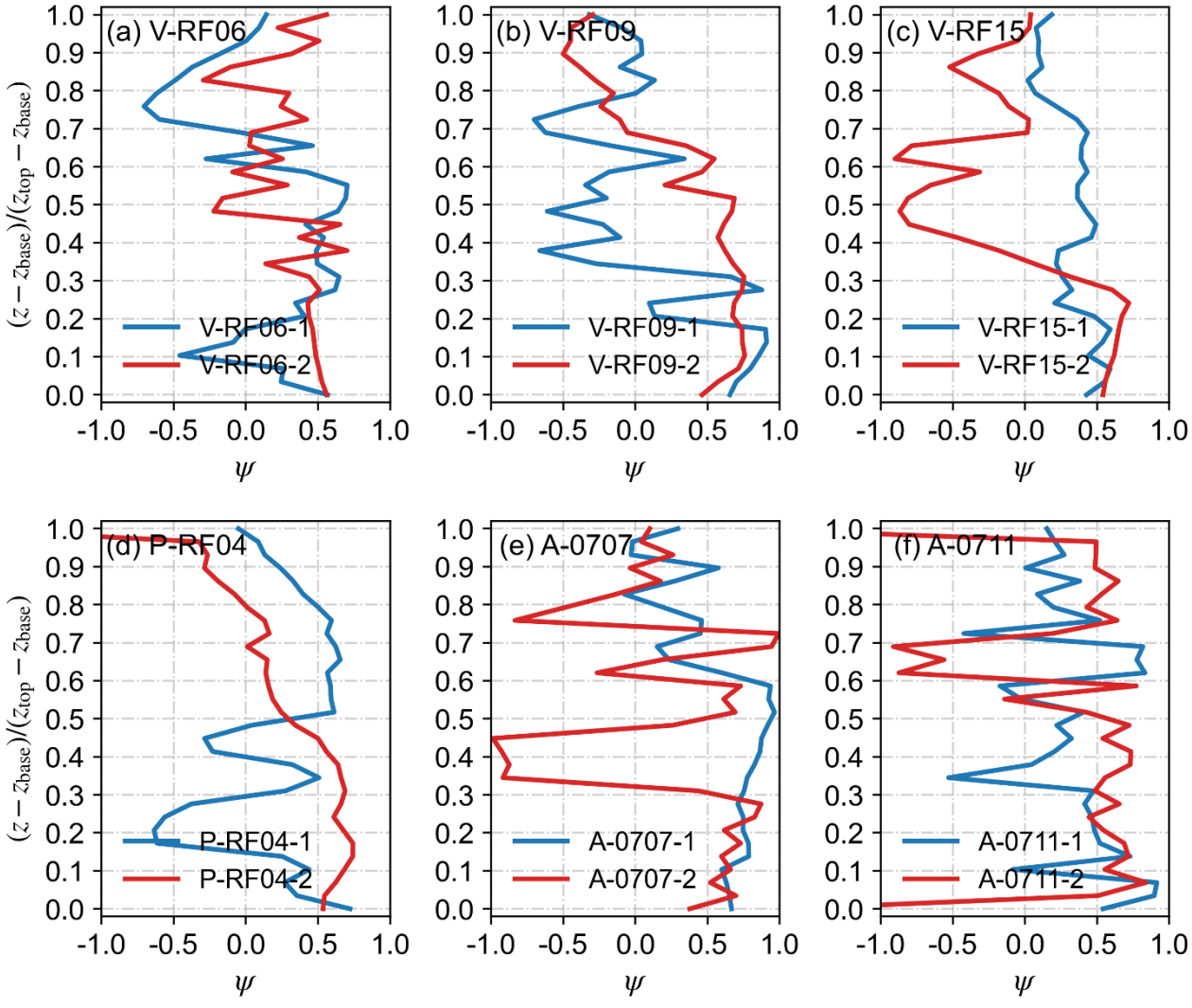

Figure 8. Vertical distributions of ψ for decoupled cases. Altitudes are normalized by the cloud layer thickness (cloud base = 0, cloud top = 1).

Mixing diagrams have been widely used to characterize the microphysical behavior of droplets during turbulent mixing events in MSC (Pawlowska et al., 2000). The horizontal axis represents droplet number concentration normalized by its adiabatic value (N_c/N_a), while the vertical axis represents mean droplet volume normalized by its adiabatic value ($V\ /\ V_a\ = {r_m}^3/{r_a}^3$), where r_a is the mean radius corresponding to the LWC_a. Figures 9 and 10 present mixing diagrams showing the relationships between N_c/N_a, ${r_m}^3/{r_a}^3$, and T_f during the persistent evolution of decoupling under conditions without and with SHIs, respectively.

Under conditions without SHIs (Fig. 9), relatively dry air was continuously entrained from above the cloud layer. As decoupling persisted, downward-developing turbulence near cloud top produced pronounced spatial inhomogeneity in the in-

https://doi.org/10.5194/egusphere-2026-3376
Preprint. Discussion started: 6 July 2026

cloud water vapor field and LWC, causing IM to dominate the mixing process. In the mixing diagrams, this process is characterized by relatively stable or only weakly varying ${r_m}^3/{r_a}^3$ as N_c/N_a decreases (Yeom et al., 2017). This behavior indicates that small droplets preferentially undergo complete evaporation during turbulent mixing, while larger droplets survive. As a result, N_c decreases substantially whereas mean droplet volume changes only slightly, representing a typical signature of selective evaporation. In the strongly turbulent upper cloud region, IM generates strong perturbations in the water vapor field and relative humidity, allowing transiently elevated supersaturation to persist locally and thereby favoring differential condensational growth of surviving droplets, ultimately promoting the formation of super-adiabatic droplets (Fig. 9a-f). This result is consistent with previous studies showing that local perturbations in LWC, water vapor, and relative humidity induced by turbulent mixing are important physical mechanisms for the formation of super-adiabatic droplets (Baker et al., 1980; Lasher-Trapp et al., 2005; Yang et al., 2016).

Because overall turbulence was relatively strong during the V-RF09 observations (Fig. 3c, d), together with relatively large T_f, the V-RF09-2 case already possessed favorable conditions for collision–coalescence growth. This finding is consistent with Chen et al. (2018), who showed that turbulence enhances collision efficiency. Under such conditions, some large droplets can grow rapidly through collision–coalescence in addition to condensational growth. Consequently, super-adiabatic droplets were also observed in the lower cloud region of V-RF09-2. By contrast, although the V-RF06 and V-RF15 flights also exhibited pronounced IM characteristics in the upper cloud region, their relatively weak in-cloud TKE limited vertical transport efficiency during the observations. As a result, super-adiabatic droplets formed near cloud top could not be effectively transported downward into the lower cloud region. Moreover, the relatively small T_f values indicate that droplet growth remained primarily controlled by condensation, with only limited contributions from collision–coalescence, explaining the absence of super-adiabatic droplets in the lower cloud regions of these flights.

Figure 10 shows that as N_c/N_a decreases, ${r_m}^3/{r_a}^3$ generally remains relatively stable or changes only slightly. This indicates that IM still dominates within cloud layers containing SHIs. At the same time, SHIs provide a relatively moist and stable water vapor environment that allows surviving droplets to more readily enter the collision–coalescence growth stage. In the mixing diagrams, this process is reflected by increasing V/V_a as N_c/N_a decreases, indicating vigorous collision–coalescence growth (Desai et al., 2019). Under these conditions, IM within the cloud favors the formation of super-adiabatic droplets, which subsequently generate downward drag effects that enhance turbulence and further promote the growth of large droplets. The gradual extension of the droplet spectra toward larger droplet sizes over time in Fig. 6g–l supports this interpretation. During the P-RF04 and A-0707 observations, super-adiabatic droplets primarily appeared in the upper cloud region closer to the SHI. In contrast, during the A-0711 observations, super-adiabatic droplets were observed in both the upper and lower cloud regions because downward-developing turbulence transported super-adiabatic droplets formed near cloud top into the lower cloud layer.

Overall, under persistently decoupled boundary-layer conditions, turbulence-induced IM provides the fundamental dynamical environment for the formation of super-adiabatic droplets. In the absence of SHIs, continuous entrainment of relatively dry air

https://doi.org/10.5194/egusphere-2026-3376
Preprint. Discussion started: 6 July 2026

causes evaporation-driven IM to dominate, resulting in substantial reductions in N_c, and an overall weakening of cloud microphysical development. In contrast, when SHIs are present, the associated moisture supply suppresses droplet evaporation and favors collision–coalescence growth. As a result, the large-droplet effect associated with IM is further amplified, substantially promoting the sustained development of warm-cloud microphysical processes.

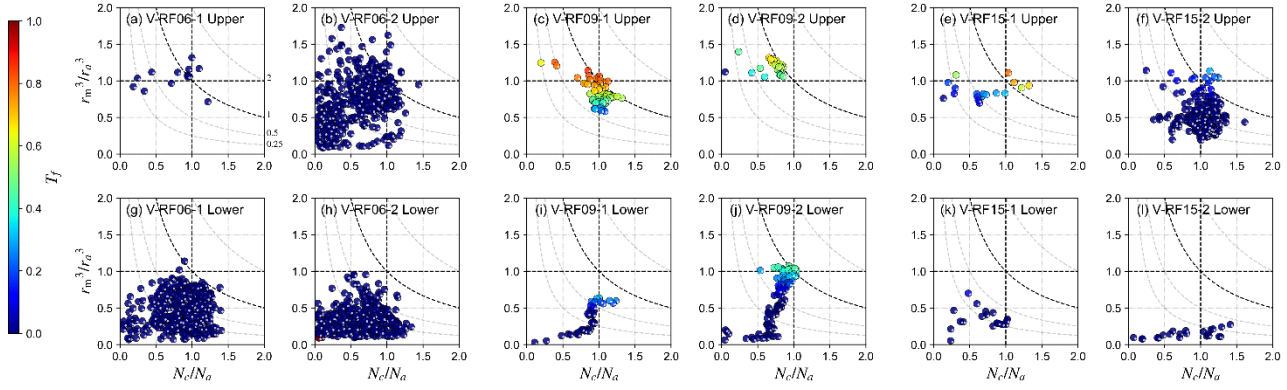

555 **Figure 9. Mixing diagrams showing normalized cloud droplet number concentration (N_c/N_a) versus normalized droplet volume(r_m^3/r_a^3) for cloud segments observed during V-RF06, V-RF09, and V-RF15. Colors indicate the collision–coalescence threshold (T_f), and dashed lines denote isolines of liquid water content (LWC).**

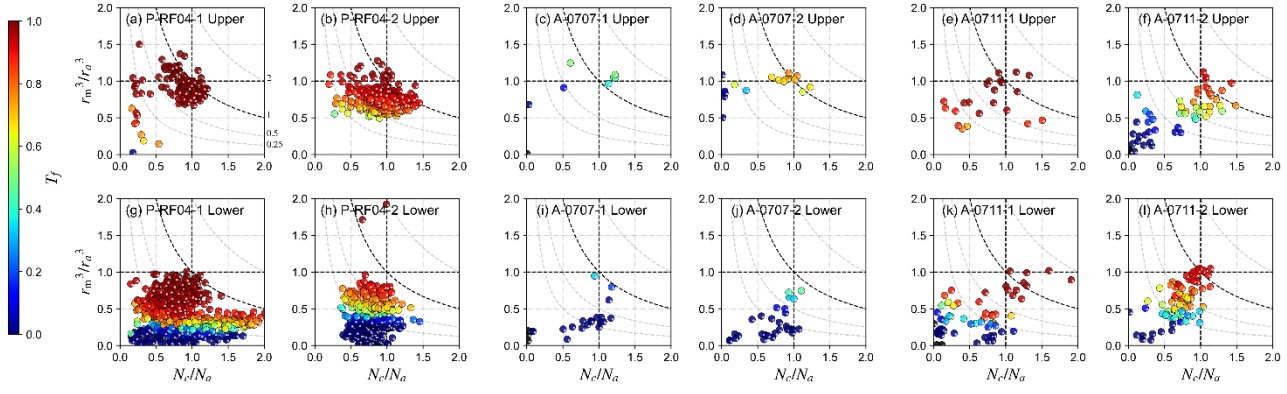

560 **Figure 10. Same as Figure 9 but for P-RF04, A-0707, and A-0711.**

3.4 Impacts of persistent decoupling on the shortwave radiative response of MSC

Figure 11 illustrates the evolutionary trajectories of all cases in the relationship between τ and $SW\ CRF_{\mathrm{TOA}}$, where marker size represents r_e, and arrows indicate the evolution from the first to the second stage within the same flight. The corresponding values of τ, r_e, ΔA, and $SW\ CRF_{\mathrm{TOA}}$ are summarized in Table 3.

565 For cases without SHIs, V-RF06 and V-RF15 exhibited generally consistent evolutionary pathways, both shifting toward the upper-left direction from the first to the second stage, corresponding to decreasing τ and weakening absolute values of $SW\ CRF_{\mathrm{TOA}}$, indicating reduced shortwave cooling. These results suggest that, in the absence of moisture buffering associated with SHIs, persistent decoupling drives the cloud system toward optical weakening accompanied by reduced radiative cooling

https://doi.org/10.5194/egusphere-2026-3376
Preprint. Discussion started: 6 July 2026

efficiency. This evolution is consistent with the previously identified cloud thinning, decreases in LWC, and narrowing droplet spectra, collectively reflecting overall cloud dissipation tendencies. Although V-RF09 also belonged to the cases without SHIs, its evolutionary pathway differed, shifting toward the lower-left direction. In this case, τ decreased while the absolute magnitude of $SW\ CRF_{\mathrm{TOA}}$ slightly increased, reflecting enhanced shortwave cooling despite cloud thinning. This result suggests that the radiative response did not weaken simultaneously with the reduction in cloud thickness. Although the reduction in total cloud water led to decreased τ, r_{e} also decreased from 7.75 to 7.04 μm (Table 3), which increased the scattering efficiency per unit cloud water and partially offset the radiative impact associated with cloud thinning. As a result, the cloud albedo was maintained or even slightly enhanced, leading to a modest increase in the magnitude of $SW\ CRF_{\mathrm{TOA}}$.

In contrast, cases with SHIs mainly exhibited two distinct evolutionary pathways. A-0707 and A-0711 both shifted toward the lower-left direction, characterized by increasing absolute values of $SW\ CRF_{\mathrm{TOA}}$ over time, corresponding to enhanced shortwave cooling. This indicates that moisture supplied by SHIs promoted cloud development and strengthened radiative cooling to some extent. Conversely, P-RF04 shifted toward the upper-left direction, with substantially reduced τ accompanied by markedly weakened shortwave cooling, consistent with the precipitation-driven removal of cloud water discussed previously for this case.

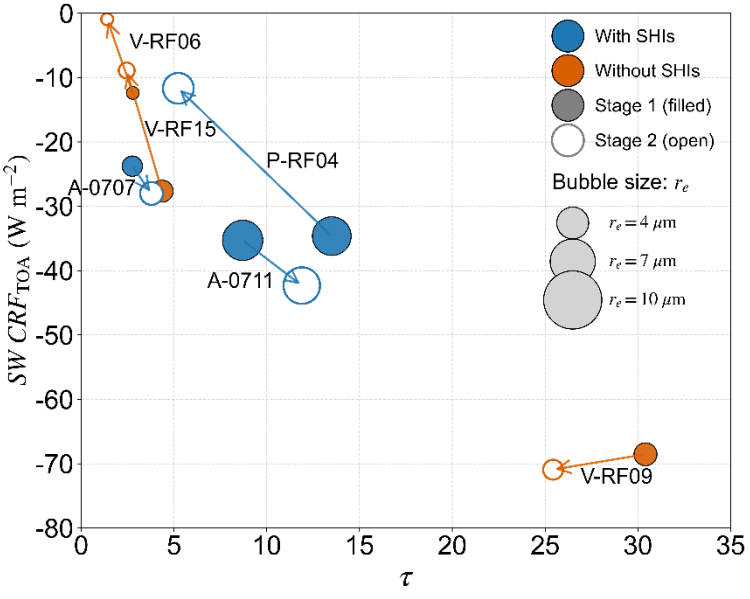

Figure 11. Evolution pathways of cloud optical thickness (τ) and top-of-atmosphere shortwave cloud radiative forcing ($SW\ CRF_{\mathrm{TOA}}$) under persistent boundary layer decoupling.

Table 3. Cloud optical depth (τ), droplet effective radius (r_{e}), albedo change (ΔA), and top-of-atmosphere shortwave cloud radiative forcing ($SW\ CRF_{\mathrm{TOA}}$) for different cases.

case	τ	r_{e} (μm)	ΔA	$SW\ CRF_{\mathrm{TOA}}$ ($W\ m^{-2}$)
V-RF06-1	2.78	5.25	0.0131	−14.51

https://doi.org/10.5194/egusphere-2026-3376
Preprint. Discussion started: 6 July 2026

V-RF06-2	1.40	5.00	0.0007	−0.94
V-RF09-1	30.41	7.75	0.0779	−68.54
V-RF09-2	25.43	7.04	0.0642	−70.92
V-RF15-1	4.36	7.53	0.0311	−27.65
V-RF15-2	2.45	6.04	0.0077	−8.89
P-RF04-1	13.50	10.98	0.0297	−34.63
P-RF04-2	5.23	9.42	0.0091	−11.67
A-0707-1	2.75	7.15	0.0311	−23.77
A-0707-2	3.79	7.73	0.0326	−28
A-0711-1	8.70	11.28	0.0494	−35.28
A-0711-2	11.89	10.57	0.0382	−42.32

Among the cases without SHIs, both V-RF06 and V-RF15 exhibited simultaneous decreases in τ, r_e, ΔA, and the absolute magnitude of $SW\ CRF_{TOA}$. Specifically, ΔA decreased from 0.0112 to 0.0007 in V-RF06 and from 0.0311 to 0.0077 in V-RF15, both corresponding to pronounced weakening of $SW\ CRF_{TOA}$ (Table 3). Notably, although r_e decreased in both cases, the reduction in τ was substantially larger. Consequently, the radiative evolution was primarily controlled by the decrease in τ, while the enhanced scattering efficiency associated with smaller r_e was insufficient to reverse the overall weakening trend. The evolution of V-RF09 differed from the other two cases without SHIs. During this flight, τ, r_e, and ΔA all decreased, indicating an overall weakening of cloud optical properties and reduced enhancement of planetary albedo by the cloud. However, $SW\ CRF_{TOA}$ slightly strengthened from –68.54 to –70.92 $W\ m^{-2}$, deviating from the behavior of ΔA. The decrease in r_e from 7.75 to 7.04 μm enhanced scattering efficiency per unit cloud water, partially compensating for the optical weakening caused by cloud thinning, thereby producing a divergence in the responses of $SW\ CRF_{TOA}$, τ, and ΔA. This result highlights that changes in droplet size can influence cloud radiative effects independently of variations in τ, partially compensating for the radiative weakening associated with cloud thinning.

For cases with SHIs, both τ and r_e increased in A-0707, while ΔA increased from 0.0311 to 0.0326, accompanied by enhanced $SW\ CRF_{TOA}$. In this case, the radiative enhancement was primarily controlled by increasing τ. Although increasing r_e theoretically reduces scattering efficiency, its influence was smaller than that of the increasing optical thickness and therefore did not alter the overall radiative enhancement trend. In A-0711, increasing τ together with decreasing r_e both favored enhanced solar scattering, resulting in strengthened $SW\ CRF_{TOA}$, consistent with the pathway shown in Figure 11. However, ΔA decreased from 0.0494 to 0.0382, indicating that although top-of-atmosphere shortwave cooling intensified, the albedo contrast between cloudy and clear-sky conditions weakened. This discrepancy may be associated with changes in the vertical cloud droplet distribution or spatial cloud inhomogeneity.

In P-RF04, τ decreased substantially from 13.50 to 5.23, while r_e decreased from 10.98 to 9.42 μm. Meanwhile, ΔA decreased from 0.0297 to 0.0091, and $SW\ CRF_{TOA}$ weakened from −34.63 to −11.67 $W\ m^{-2}$. Overall, the cloud exhibited weakened

https://doi.org/10.5194/egusphere-2026-3376
Preprint. Discussion started: 6 July 2026

enhancement of planetary albedo and substantially reduced shortwave cooling at the top of the atmosphere. The formation of large droplets reduced scattering efficiency per unit cloud water and weakened cloud albedo, while simultaneously accelerating precipitation processes that removed large amounts of cloud water from the cloud system. As a result, the cloud experienced both optical weakening and shortened lifetime, further suppressing shortwave cooling.

Overall, for most cases, changes in $SW\ CRF_{\mathrm{TOA}}$ were broadly consistent with changes in τ, while variations in r_{e} modulated this relationship through their influence on scattering efficiency. In V-RF09, this modulation was sufficiently strong to produce a clear divergence between the responses of $SW\ CRF_{\mathrm{TOA}}$ and τ. Under conditions without SHIs, the relationship between cloud dissipation and weakened shortwave cooling was relatively direct. Under conditions with SHIs, the additional moisture supply partially buffered the dissipative effects associated with persistent decoupling. Nevertheless, the ultimate radiative evolution remained strongly dependent on the subsequent microphysical evolution of the cloud, particularly the balance between cloud-water maintenance and cloud-water loss associated with droplet growth processes. These radiative response differences, jointly modulated by boundary-layer decoupling state, cloud-top humidity structure, and in-cloud microphysical processes, represent an important source of uncertainty in low-cloud shortwave radiative feedbacks, highlighting the need for improved observational constraints on MSC microphysical and radiative processes in climate model parameterizations.

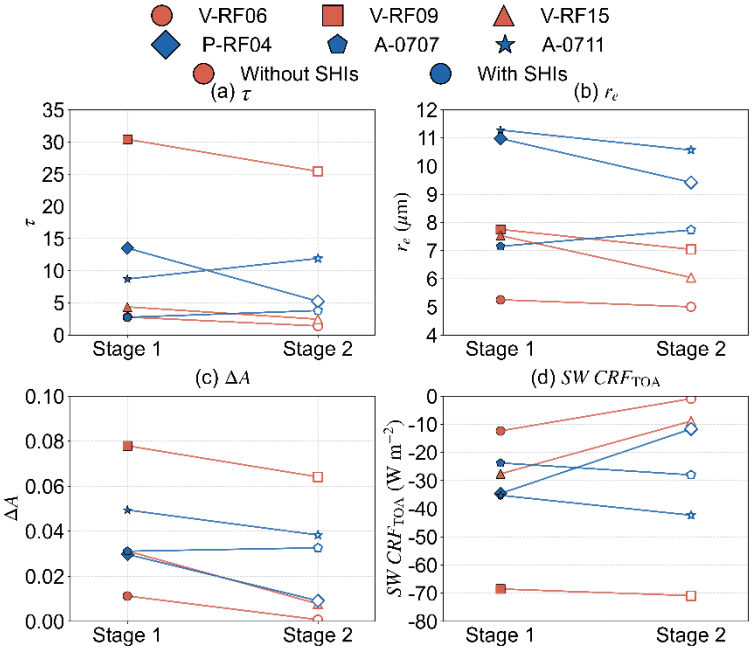

Figure 12. Case-to-case changes in cloud optical and radiative properties (τ, ΔA, r_{e} and $SW\ CRF_{\mathrm{TOA}}$) during persistent boundary layer decoupling.

https://doi.org/10.5194/egusphere-2026-3376
Preprint. Discussion started: 6 July 2026

4 Discussion and conclusions

Based on aircraft in situ observations, this study selected six flights (V-RF06, V-RF09, V-RF15, P-RF04, A-0707, and A-0711), comprising a total of twelve MSC cases under persistently decoupled conditions. The study systematically investigated the evolution of MSC microphysical properties, in-cloud mixing processes, and shortwave radiative responses under persistent boundary-layer decoupling, with particular emphasis on the modulating role of SHIs. The major conclusions are summarized as follows.

Persistent boundary-layer decoupling generally suppresses the maintenance and development of MSC. Under conditions without SHIs (V-RF06, V-RF09, and V-RF15), the cloud layers generally evolved toward reduced thickness, decreased LWC, and narrowed droplet spectra over time. Dissipation of small cloud droplets induced by entrainment evaporation of dry free-tropospheric air near cloud top became the dominant process. This result is consistent with previous studies indicating that entrainment of dry free-tropospheric air enhances drying through entrainment and accelerates cloud water loss (Zhang et al., 2026). The present study further provides observational evidence from the perspectives of droplet spectrum narrowing and the evolution of IM characteristics. Meanwhile, the cloud mixing process was dominated by IM, characterized by substantial decreases in N_c over time while the mean droplet volume remained relatively unchanged. Negative ψ values occurred most frequently near cloud top, indicating persistent IM-dominated conditions accompanied by super-adiabatic droplets, whereas ψ in the lower cloud region generally remained positive and exhibited only small temporal variations as decoupling persisted. Near cloud top, strong turbulence maintained instantaneous localized supersaturation, allowing surviving droplets to undergo differential condensational growth and form super-adiabatic droplets, consistent with the findings of Baker et al. (1980) and Yang et al. (2016), who emphasized that turbulence-induced localized supersaturation perturbations constitute an important mechanism for super-adiabatic droplet formation. This dissipative process exhibited clear vertical heterogeneity, with the strongest entrainment influence occurring near cloud top, whereas changes in the lower cloud layer were comparatively weaker, reflecting a top-down dissipation process under persistently decoupled conditions. In terms of radiative effects, the microphysical weakening ultimately manifested as simultaneous decreases in τ, r_e, and ΔA, accompanied by weakened $SW\ CRF_{TOA}$. However, during the V-RF09 observations, relatively strong TKE promoted more active collision–coalescence growth within the cloud, and super-adiabatic droplets were also observed in the lower cloud layer. The decrease in r_e enhanced the scattering efficiency per unit cloud water, leading to a slight increase in the absolute magnitude of $SW\ CRF_{TOA}$ despite the simultaneous reduction in τ. This result highlights that variations in droplet size can modulate cloud radiative responses and partially compensate for the radiative weakening associated with cloud thinning, although they do not alter the overall tendency for persistent decoupling to drive cloud dissipation.

The presence of SHIs (P-RF04, A-0707, and A-0711) systematically modified the effects of persistent decoupling and altered the evolutionary pathways. From a microphysical perspective, continuous moisture supply from SHIs effectively suppressed entrainment evaporation and slowed the decline of cloud microphysical quantities, while the cloud droplet spectra systematically broadened toward larger droplet sizes over time. Regarding mixing characteristics, the additional moisture input

https://doi.org/10.5194/egusphere-2026-3376
Preprint. Discussion started: 6 July 2026

modified the microphysical consequences of IM by suppressing droplet evaporation, enhancing collision–coalescence growth, and promoting broader droplet spectra. In the mixing diagrams, this process was reflected by decreasing N_c/N_a accompanied by increasing ${r_m}^3/{r_a}^3$, indicating active collision–coalescence growth (Desai et al., 2019). The combined effects of IM and moisture supply promoted the formation of super-adiabatic droplets, while the downward drag induced by these large droplets further enhanced local turbulence, forming a positive feedback mechanism. In terms of radiative effects, this microphysical maintenance and development corresponded to enhanced $SW\ CRF_{TOA}$ in A-0707 and A-0711. Under conditions where SHIs remained continuously connected to cloud top and moisture supply was sufficiently strong (A-0711), moisture input was gradually transported downward into the cloud layer, leading to increases in LWC and N_c in the lower cloud region. In this case, SHIs not only delayed cloud dissipation but also actively promoted cloud redevelopment. However, the influence of SHIs on persistent decoupling did not simply enhance cloud maintenance. When collision–coalescence growth became sufficiently strong to initiate precipitation (P-RF04), substantial cloud water was removed through precipitation processes, resulting in simultaneous large decreases in both τ and $SW\ CRF_{TOA}$, thereby producing an alternative dissipation pathway dominated by precipitation removal. These results indicate that SHIs can fundamentally modify the microphysical evolution pathway of decoupled MSC by suppressing entrainment-driven evaporation and promoting collision–coalescence growth. Depending on the subsequent cloud evolution, this process may either support cloud maintenance and redevelopment or, when droplet growth becomes sufficiently strong, contribute to cloud-water loss through precipitation-related removal processes. The ultimate outcome depends on the balance among entrainment-driven evaporation, SHI-associated moisture supply, and cloud-water loss through precipitation-related processes, consistent with previous studies emphasizing the competing influences of these mechanisms on cloud evolution (Zhang et al., 2026). The major processes identified in this study are summarized schematically in Figure 13.

From a climatic perspective, the present results demonstrate that MSC shortwave radiative effects are not stable under persistently decoupled conditions. The three distinct evolutionary pathways identified in this study – evaporative dissipation, redevelopment, and precipitation-driven dissipation – can produce substantially different radiative responses. Even under similar decoupled boundary-layer conditions, differences in cloud-top humidity structure and in-cloud turbulence characteristics can lead clouds to evolve along markedly different pathways. Therefore, more consistent representation of the coupled effects among boundary-layer decoupling, cloud-top humidity structure, and cloud microphysical processes in climate models is essential for constraining uncertainties in low-cloud shortwave radiative feedbacks. This study is based on a limited number of observational cases, and the selected flights originated from different field campaigns with differing environmental backgrounds. Consequently, the statistical robustness of these conclusions requires further validation with larger observational samples. Future work should combine targeted large-eddy simulations with systematic numerical experiments on humidity inversion–mixing–microphysics interactions under persistently decoupled conditions, and extend the analysis to larger observational samples to evaluate the generality of the present findings and provide improved observational constraints for low-cloud shortwave radiative feedback parameterizations in climate models.

https://doi.org/10.5194/egusphere-2026-3376
Preprint. Discussion started: 6 July 2026

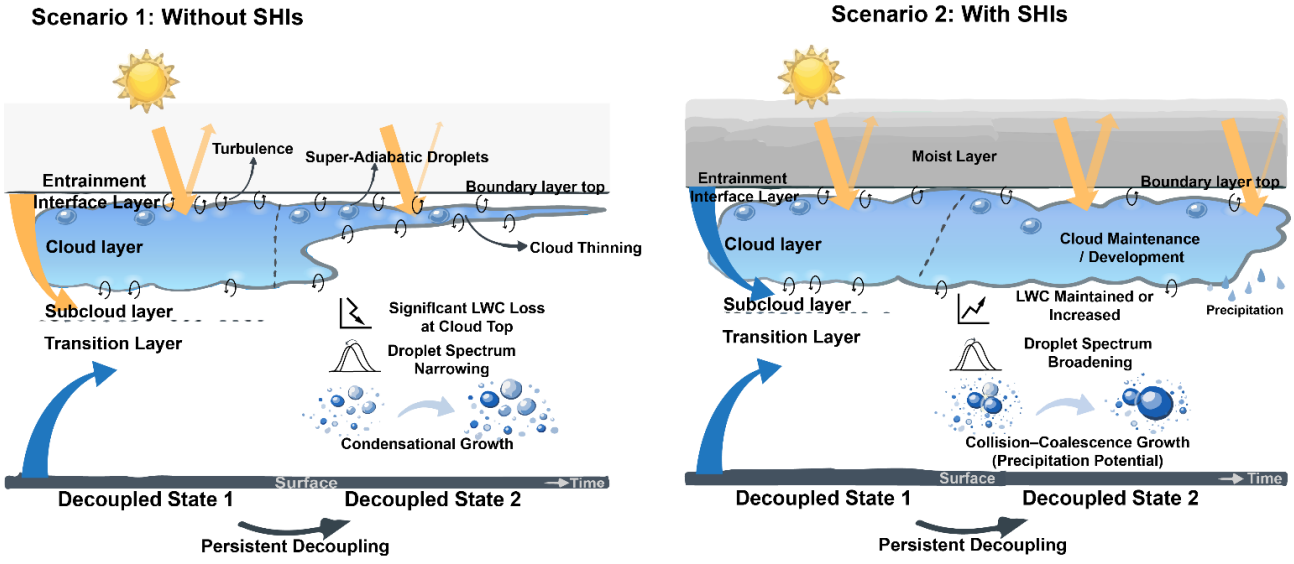

Figure 13. Conceptual schematic of the evolutionary processes of marine stratocumulus clouds (MSC) under conditions without (left panel) and with (right panel) specific humidity inversions (SHIs) near cloud top. Curved arrows on the left side of each panel represent turbulent mixing, with arrow width indicating turbulent kinetic energy (*TKE*) intensity: upward arrows (blue) originate from surface-driven fluxes, while downward arrows indicate cloud-top entrainment, shown in yellow for the no-SHI case and blue for the SHI case, representing dry-air and moist-air entrainment, respectively. Large blue droplets within the cloud layer represent super-adiabatic droplets. Partially whitened regions with small recirculating arrows indicate localized inhomogeneous mixing. Paired yellow arrows near cloud top denote shortwave radiation, with arrow thickness reflecting the evolution of cloud reflectivity.

Code availability

Code is available from the corresponding author upon reasonable request.

Data availability

The observational datasets used in this study are publicly available from third-party repositories. VOCALS-REx aircraft data, including 40 Hz boundary-layer turbulence data (Khelif, 2011; https://doi.org/10.26023/H6EE-YRXP-YD00), 1 Hz CAPS probe microphysical data (Albrecht, 2011a; https://doi.org/10.26023/X68G-FQPT-ZN00), and 1 Hz navigation and state parameter data (Albrecht, 2011b; https://doi.org/10.26023/36PD-HZKW-RJ03), are archived at the UCAR/NCAR Earth Observing Laboratory (EOL; https://data.eol.ucar.edu/). POST aircraft data, including 40 Hz turbulence data (Khelif, 2009; https://doi.org/10.26023/XF1E-R6W2-2N0Z), 1 Hz CAS drop size spectra (Jonsson, 2009a; https://doi.org/10.26023/2KKX-GWDR-RX0V), and 1 Hz navigation, state parameter, and microphysics data (Jonsson, 2009b; https://doi.org/10.26023/7WRV-918Y-X10G), are also publicly available from UCAR/NCAR EOL. The EOL Field Catalog is available at https://doi.org/10.5065/D6SQ8XFB (NSF NCAR – Earth Observing Laboratory, 1995–present). ACE-ENA AIMMS-20 20 Hz wind and thermodynamic data and FCDP 1 Hz cloud microphysical data are publicly available from the ARM Data Center (https://www.arm.gov/data). The data produced in the study are available from the corresponding author upon reasonable request.

https://doi.org/10.5194/egusphere-2026-3376
Preprint. Discussion started: 6 July 2026

Author contributions

JZ and SY jointly conceived this study. Data curation and collection were performed by JZ, SY, and MG. JZ and SY carried out the data analysis and radiative transfer calculations. MG contributed to data processing and analysis. JL assisted with the analysis and participated in discussions of the results. JZ was responsible for data interpretation and figure preparation. The initial draft was prepared by JZ and SY, with input from MG and JL. CL and YP provided scientific guidance, contributed to the interpretation of the results, and critically reviewed the methodology and manuscript. All authors reviewed and approved the final manuscript.

Competing interests

The authors declare that they have no conflict of interest.

Disclaimer

Copernicus Publications adds a standard disclaimer: “Copernicus Publications remains neutral with regard to jurisdictional claims made in the text, published maps, institutional affiliations, or any other geographical representation in this paper. While Copernicus Publications makes every effort to include appropriate place names, the final responsibility lies with the authors. Views expressed in the text are those of the authors and do not necessarily reflect the views of the publisher.”

Acknowledgements

The authors gratefully acknowledge the VOCALS-REx, POST, and ACE-ENA field campaigns for conducting the aircraft measurements and making the high-quality datasets publicly available. We thank the principal investigators, instrument teams, data managers, and support staff from the UCAR/NCAR Earth Observing Laboratory (EOL) and the Atmospheric Radiation Measurement (ARM) Data Center for their dedicated efforts in data collection, quality control, and archiving. The authors also acknowledge the computational resources provided by the university servers of Nanjing University of Information Science and Technology, which were used to run the Santa Barbara DISORT Atmospheric Radiative Transfer (SBDART) model simulations.

https://doi.org/10.5194/egusphere-2026-3376
Preprint. Discussion started: 6 July 2026

Financial support

This research was supported by the National Key Research and Development Program of China (grant no. 2017YFC1501404) and the National Natural Science Foundation of China (grant no. 41575133).

References

Albrecht, B.: VOCALS: CIRPAS Twin Otter CAPS Probe Data. Version 1.0 [data set], UCAR/NCAR – Earth Observing Laboratory, https://doi.org/10.26023/X68G-FQPT-ZN00, 2011a.

Albrecht, B.: VOCALS: CIRPAS Twin Otter Navigation and State Parameters. Version 1.0 [data set], UCAR/NCAR – Earth Observing Laboratory, https://doi.org/10.26023/36PD-HZKW-RJ03, 2011b.

Albrecht, B. A., Jensen, M. P., and Syrett, W. J.: Marine boundary layer structure and fractional cloudiness, J. Geophys. Res. Atmos., 100, 14209–14222, https://doi.org/10.1029/95JD00827, 1995.

Baker, M. B., Corbin, R. G., and Latham, J.: The influence of entrainment on the evolution of cloud droplet spectra: I. A model of inhomogeneous mixing, Q.J.R. Meteorol. Soc., 106, 581–598, https://doi.org/10.1002/qj.49710644914, 1980.

Bolton, D.: The computation of equivalent potential temperature, Mon. Wea. Rev., 108, 1046–1053, https://doi.org/10.1175/1520-0493(1980)108<1046:TCOEPT>2.0.CO;2, 1980.

Bretherton, C. S. and Wyant, M. C.: Moisture transport, lower-tropospheric stability, and decoupling of cloud-topped boundary layers, J. Atmos. Sci., https://doi.org/10.1175/1520-0469(1997)054<0148:MTLTSA>2.0.CO;2, 1997.

Bretherton, C. S., Uttal, T., Fairall, C. W., Yuter, S. E., Weller, R. A., Baumgardner, D., Comstock, K., Wood, R., and Raga, G. B.: The EPIC 2001 stratocumulus study, Bull. Am. Meteorol. Soc., 85, 967–978, https://doi.org/10.1175/BAMS-85-7-967, 2004.

Bretherton, C. S., Uchida, J., and Blossey, P. N.: Slow manifolds and multiple equilibria in stratocumulus-capped boundary layers, J Adv Model Earth Syst, 2, 14, https://doi.org/10.3894/JAMES.2010.2.14, 2010.

Brunke, M. A., Cutler, L., Urzua, R. D., Corral, A. F., Crosbie, E., Hair, J., Hostetler, C., Kirschler, S., Larson, V., Li, X., Ma, P., Minke, A., Moore, R., Robinson, C. E., Scarino, A. J., Schlosser, J., Shook, M., Sorooshian, A., Lee Thornhill, K., Voigt, C., Wan, H., Wang, H., Winstead, E., Zeng, X., Zhang, S., and Ziemba, L. D.: Aircraft observations of turbulence in cloudy and cloud-free boundary layers over the western North Atlantic Ocean from ACTIVATE and implications for the Earth system model evaluation and development, J. Geophys. Res. Atmos., 127, e2022JD036480, https://doi.org/10.1029/2022JD036480, 2022.

Cess, R. D., Potter, G. L., Blanchet, J. P., Boer, G. J., Ghan, S. J., Kiehl, J. T., Le Treut, H., Li, Z.-X., Liang, X.-Z., Mitchell, J. F. B., Morcrette, J.-J., Randall, D. A., Riches, M. R., Roeckner, E., Schlese, U., Slingo, A., Taylor, K. E., Washington, W.

https://doi.org/10.5194/egusphere-2026-3376
Preprint. Discussion started: 6 July 2026

M., Wetherald, R. T., and Yagai, I.: Interpretation of cloud-climate feedback as produced by 14 atmospheric general circulation models, Science, 245, 513–516, https://doi.org/10.1126/science.245.4917.513, 1989.

Chechin, D. G., Lüpkes, C., Hartmann, J., Ehrlich, A., and Wendisch, M.: Turbulent structure of the Arctic boundary layer in early summer driven by stability, wind shear and cloud-top radiative cooling: ACLOUD airborne observations, Atmos. Chem. Phys., 23, 4685–4707, https://doi.org/10.5194/acp-23-4685-2023, 2023.

Chen, S., Yau, M.-K., Bartello, P., and Xue, L.: Bridging the condensation–collision size gap: a direct numerical simulation of continuous droplet growth in turbulent clouds, Atmos. Chem. Phys., 18, 7251–7262, https://doi.org/10.5194/acp-18-7251-2018, 2018.

Chen, T., Rossow, W. B., and Zhang, Y.: Radiative effects of cloud-type variations, J. Clim., 13, 264–286, https://doi.org/10.1175/1520-0442(2000)013<0264:REOCTV>2.0.CO;2, 2000.

Considine, G. D.: Modeling the diurnal variability in cloud microphysics in boundary layer clouds, J. Geophys. Res. Atmos., 102, 1717–1726, https://doi.org/10.1029/96JD02997, 1997.

Desai, N., Glienke, S., Fugal, J., and Shaw, R. A.: Search for Microphysical Signatures of Stochastic Condensation in Marine Boundary Layer Clouds Using Airborne Digital Holography, J. Geophys. Res. Atmos., 124, 2739–2752, https://doi.org/10.1029/2018JD029033, 2019.

Desai, N., Liu, Y., Glienke, S., Shaw, R. A., Lu, C., Wang, J., and Gao, S.: Vertical variation of turbulent entrainment mixing processes in marine stratocumulus clouds using high-resolution digital holography, J. Geophys. Res. Atmos., 126, e2020JD033527, https://doi.org/10.1029/2020JD033527, 2021.

Dodson, D. S. and Small Griswold, J. D.: Turbulent and boundary layer characteristics during VOCALS-REx, Atmos. Chem. Phys., 21, 1937–1961, https://doi.org/10.5194/acp-21-1937-2021, 2021.

Driedonks, A. G. M. and Duynkerke, P. G.: Current problems in the stratocumulus-topped atmospheric boundary layer, Boundary-Layer Meteorol, 46, 275–303, https://doi.org/10.1007/BF00120843, 1989.

Duda, D. P., Stephens, G. L., and Cox, S. K.: Microphysical and radiative properties of marine stratocumulus from tethered balloon measurements, J. Appl. Meteor., 30, 170–186, https://doi.org/10.1175/1520-0450(1991)030<0170:MARPOM>2.0.CO;2, 1991.

Eastman, R. and Wood, R.: The Competing Effects of Stability and Humidity on Subtropical Stratocumulus Entrainment and Cloud Evolution from a Lagrangian Perspective, J. Atmos. Sci., 75, 2563–2578, https://doi.org/10.1175/JAS-D-18-0030.1, 2018.

Egerer, U., Ehrlich, A., Gottschalk, M., Griesche, H., Neggers, R. A. J., Siebert, H., and Wendisch, M.: Case study of a humidity layer above Arctic stratocumulus and potential turbulent coupling with the cloud top, Atmos. Chem. Phys., 21, 6347–6364, https://doi.org/10.5194/acp-21-6347-2021, 2021.

Gerber, H., Frick, G., Malinowski, S. P., Kumala, W., and Krueger, S.: POST - A New Look at Stratocumulus, 13th Conf. on Cloud Physics, Portland, OR, 28 June–2 July 2010, http://ams.confex.com/ams/pdfpapers/170431.pdf, 2010.

Gerber, H., Malinowski, S. P., and Jonsson, H.: Evaporative and Radiative Cooling in POST Stratocumulus, J. Atmos. Sci., 73, 3877–3884, https://doi.org/10.1175/JAS-D-16-0023.1, 2016.

https://doi.org/10.5194/egusphere-2026-3376
Preprint. Discussion started: 6 July 2026

Gerber, H. E., Frick, G. M., Jensen, J. B., and Hudson, J. G.: Entrainment, mixing, and microphysics in trade-wind cumulus, J. Meteorol. Soc. Jpn., 86A, 87–106, https://doi.org/10.2151/jmsj.86A.87, 2008.

Glassmeier, F. and Feingold, G.: Network approach to patterns in stratocumulus clouds, Proc. Natl. Acad. Sci. U.S.A., 114, 10578–10583, https://doi.org/10.1073/pnas.1706495114, 2017.

Goren, T., Rosenfeld, D., Sourdeval, O., and Quaas, J.: Satellite observations of precipitating marine stratocumulus show greater cloud fraction for decoupled clouds in comparison to coupled clouds, Geophys. Res. Lett., 45, 5126–5134, https://doi.org/10.1029/2018GL078122, 2018.

Greenwald, T. J. and Christopher, S. A.: The GOES I–M imagers: New tools for studying microphysical properties of boundary layer stratiform clouds, Bull. Amer. Meteor. Soc., 81, 2607–2620, https://doi.org/10.1175/1520-0477(2000)081<2607:TGIINT>2.3.CO;2, 2000.

Hahn, C. J. and Warren, S. G.: A gridded climatology of clouds over land (1971–1996) and ocean (1954–2008) from surface observations worldwide (NDP-026E), Carbon Dioxide Information Analysis Center, Oak Ridge National Laboratory [data set], https://doi.org/10.3334/CDIAC/CLI.NDP026E, 2007.

Hartmann, D. L. and Short, D. A.: On the use of Earth radiation budget statistics for studies of clouds and climate, J. Atmos. Sci., 37, 1233–1250, https://doi.org/10.1175/1520-0469(1980)037<1233:OTUOER>2.0.CO;2, 1980.

Hartmann, D. L., Ockert-Bell, M. E., and Michelsen, M. L.: The effect of cloud type on Earth's energy balance: Global analysis, J. Clim., 5, 1281–1304, https://doi.org/10.1175/1520-0442(1992)005<1281:TEOCTO>2.0.CO;2, 1992.

Jones, C. R., Bretherton, C. S., and Leon, D.: Coupled vs. decoupled boundary layers in VOCALS-REx, Atmos. Chem. Phys., 11, 7143–7153, https://doi.org/10.5194/acp-11-7143-2011, 2011.

Jonsson, H.: POST: CIRPAS Twin Otter 1-hz CAS Drop Size Spectra. Version 1.0 [data set], UCAR/NCAR – Earth Observing Laboratory, https://doi.org/10.26023/2KKX-GWDR-RX0V, 2009a.

Jonsson, H.: POST: CIRPAS Twin Otter 1-hz Navigation, State Parameter, and Microphysics Flight-Level Data - ASCII format. Version 1.0 [data set], UCAR/NCAR – Earth Observing Laboratory, https://doi.org/10.26023/7WRV-918Y-X10G, 2009b.

Khelif, D.: POST: UC Irvine 40-hz Probes - ASCII format. Version 1.0 [data set], UCAR/NCAR – Earth Observing Laboratory, https://doi.org/10.26023/XF1E-R6W2-2N0Z, 2009.

Khelif, D.: VOCALS: CIRPAS Twin Otter 40 Hz Boundary Layer Turbulence Data. Version 1.0 [data set], UCAR/NCAR – Earth Observing Laboratory, https://doi.org/10.26023/H6EE-YRXP-YD00, 2011.

Klein, S. A. and Hartmann, D. L.: The seasonal cycle of low stratiform clouds, J. Climate, 6, 1587–1606, https://doi.org/10.1175/1520-0442(1993)006<1587:TSCOLS>2.0.CO;2, 1993.

Lasher-Trapp, S. G., Cooper, W. A., and Blyth, A. M.: Broadening of droplet size distributions from entrainment and mixing in a cumulus cloud, Q. J. R. Meteorol. Soc., 131, 195–220, https://doi.org/10.1256/qj.03.199, 2005.

Lilly, D. K.: Models of cloud-topped mixed layers under a strong inversion, Q. J. R. Meteorol. Soc., 94, 292–309, https://doi.org/10.1002/qj.49709440106, 1968.

https://doi.org/10.5194/egusphere-2026-3376
Preprint. Discussion started: 6 July 2026

Mellado, J. P.: Cloud-top entrainment in stratocumulus clouds, Annu. Rev. Fluid Mech., 49, 145–169, https://doi.org/10.1146/annurev-fluid-010816-060231, 2017.

Nicholls, S.: The dynamics of stratocumulus: Aircraft observations and comparisons with a mixed layer model, Q. J. R. Meteorol. Soc., 110, 783–820, https://doi.org/10.1002/qj.49711046603, 1984.

Nicholls, S. and Leighton, J.: An observational study of the structure of stratiform cloud sheets: Part I. Structure, Q. J. Roy. Meteor. Soc., 112, 431–460, https://doi.org/10.1002/qj.49711247209, 1986.

Nowak, J. L., Siebert, H., Szodry, K.-E., and Malinowski, S. P.: Coupled and decoupled stratocumulus-topped boundary layers: turbulence properties, Atmos. Chem. Phys., 21, 10965–10991, https://doi.org/10.5194/acp-21-10965-2021, 2021.

NSF NCAR – Earth Observing Laboratory: EOL Field Catalog, https://doi.org/10.5065/D6SQ8XFB, 1995–present.

Pawlowska, H., Brenguier, J. L., and Burnet, F.: Microphysical properties of stratocumulus clouds, Atmos. Res., 55, 15–33, https://doi.org/10.1016/S0169-8095(00)00054-5, 2000.

Prabhakaran, P., Shawon, A. S. M., Kinney, G., Thomas, S., Cantrell, W., and Shaw, R. A.: The role of turbulent fluctuations in aerosol activation and cloud formation, Proc. Natl. Acad. Sci. U.S.A., 117, 16831–16838, https://doi.org/10.1073/pnas.2006426117, 2020.

Ricchiazzi, P., Yang, S., Gautier, C., and Sowle, D.: SBDART: A research and teaching software tool for plane-parallel radiative transfer in the Earth's atmosphere, Bull. Amer. Meteor. Soc., 79, 2101–2114, https://doi.org/10.1175/1520-0477(1998)079<2101:SARATS>2.0.CO;2, 1998.

Shin, S.-H. and Ha, K.-J.: Implementation of turbulent mixing over a stratocumulus-topped boundary layer and its impact in a GCM, Adv. Atmos. Sci., 26, 995–1004, https://doi.org/10.1007/s00376-009-8145-0, 2009.

Siebert, H., Szodry, K.-E., Egerer, U., Wehner, B., Henning, S., Chevalier, K., Lückerath, J., Welz, O., Weinhold, K., Lauermann, F., Gottschalk, M., Ehrlich, A., Wendisch, M., Fialho, P., Roberts, G., Allwayin, N., Schum, S., Shaw, R. A., Mazzoleni, C., Mazzoleni, L., Nowak, J. L., Malinowski, S. P., Karpinska, K., Kumala, W., Czyzewska, D., Luke, E. P., Kollias, P., Wood, R., and Mellado, J. P.: Observations of Aerosol, Cloud, Turbulence, and Radiation Properties at the Top of the Marine Boundary Layer over the Eastern North Atlantic Ocean: The ACORES Campaign, Bull. Am. Meteorol. Soc., 102, E123–E147, https://doi.org/10.1175/BAMS-D-19-0191.1, 2021.

Slingo, A.: Sensitivity of the Earth's radiation budget to changes in low clouds, Nature, 343, 49–51, https://doi.org/10.1038/343049a0, 1990.

Slingo, A., Nicholls, S., and Schmetz, J.: Aircraft observations of marine stratocumulus during JASIN, Q.J.R. Meteorol. Soc., 108, 833–856, https://doi.org/10.1002/qj.49710845807, 1982.

Stephens, G. L. and Greenwald, T. J.: The Earth's radiation budget and its relation to atmospheric hydrology: 2. Observations of cloud effects, J. Geophys. Res., 96, 15325–15340, https://doi.org/10.1029/91JD00972, 1991.

Stevens, B.: Cloud transitions and decoupling in shear-free stratocumulus-topped boundary layers, Geophys. Res. Lett., 27, 2557–2560, https://doi.org/10.1029/1999GL011257, 2000.

Stevens, B.: Entrainment in stratocumulus-topped mixed layers, Q. J. R. Meteorol. Soc., 128, 2663–2690, https://doi.org/10.1256/qj.01.202, 2002.

https://doi.org/10.5194/egusphere-2026-3376
Preprint. Discussion started: 6 July 2026

Twomey, S.: Pollution and the planetary albedo, Atmos. Environ., 8, 1251–1256, https://doi.org/10.1016/0004-6981(74)90004-3, 1974.

Wang, J., Wood, R., Jensen, M. P., Chiu, J. C., Liu, Y., Lamer, K., Desai, N., Giangrande, S. E., Knopf, D. A., and Kollias, P.: Aerosol and cloud experiments in the Eastern North Atlantic (ACE-ENA), Bull. Amer. Meteor. Soc., 103, E619–E641, https://doi.org/10.1175/BAMS-D-19-0220.1, 2022.

Wang, Z., Zhang, H., and Lu, P.: Improvement of cloud microphysics in the aerosol-climate model BCC_AGCM2.0.1_CUACE/Aero, evaluation against observations, and updated aerosol indirect effect, J. Geophys. Res. Atmos., 119, 8400–8417, https://doi.org/10.1002/2014JD021886, 2014.

Warner, J.: The microstructure of cumulus cloud: Part IV. The effect on the droplet spectrum of mixing between cloud and environment, J. Atmos. Sci., 30, 256–261, https://doi.org/10.1175/1520-0469(1973)030<0256:TMOCCP>2.0.CO;2, 1973.

Wood, R.: Stratocumulus clouds, Mon. Wea. Rev., 140, 2373–2423, https://doi.org/10.1175/MWR-D-11-00121.1, 2012.

Wood, R. and Hartmann, D. L.: Spatial variability of liquid water path in marine low cloud: The importance of mesoscale cellular convection, J. Climate, 19, 1748–1764, https://doi.org/10.1175/JCLI3702.1, 2006.

Wood, R., Mechoso, C. R., Bretherton, C. S., Weller, R. A., Huebert, B., Straneo, F., Albrecht, B. A., Coe, H., Allen, G., Vaughan, G., Daum, P., Fairall, C., Chand, D., Gallardo Klenner, L., Garreaud, R., Grados, C., Covert, D. S., Bates, T. S., Krejci, R., Russell, L. M., de Szoeke, S., Brewer, A., Yuter, S. E., Springston, S. R., Chaigneau, A., Toniazzo, T., Minnis, P., Palikonda, R., Abel, S. J., Brown, W. O. J., Williams, S., Fochesatto, J., Brioude, J., and Bower, K. N.: The VAMOS Ocean-Cloud-Atmosphere-Land Study Regional Experiment (VOCALS-REx): goals, platforms, and field operations, Atmos. Chem. Phys., 11, 627–654, https://doi.org/10.5194/acp-11-627-2011, 2011.

Xiao, H., Wu, C.-M., and Mechoso, C. R.: Buoyancy reversal, decoupling and the transition from stratocumulus to shallow cumulus topped marine boundary layers, Clim Dyn, 37, 971–984, https://doi.org/10.1007/s00382-010-0882-3, 2011.

Xu, X., Lu, C., Liu, Y., Luo, S., Zhou, X., Endo, S., Zhu, L., and Wang, Y.: Influences of an entrainment–mixing parameterization on numerical simulations of cumulus and stratocumulus clouds, Atmos. Chem. Phys., 22, 5459–5475, https://doi.org/10.5194/acp-22-5459-2022, 2022.

Yang, F., Shaw, R., and Xue, H.: Conditions for super-adiabatic droplet growth after entrainment mixing, Atmos. Chem. Phys., 16, 9421–9433, https://doi.org/10.5194/acp-16-9421-2016, 2016.

Yeom, J. M., Yum, S. S., Liu, Y., and Lu, C.: A study on the entrainment and mixing process in the continental stratocumulus clouds measured during the RACORO campaign, Atmos. Res., 194, 89–99, https://doi.org/10.1016/j.atmosres.2017.04.028, 2017.

Yeom, J. M., Yum, S. S., Shaw, R. A., La, I., Wang, J., Lu, C., Liu, Y., Mei, F., Schmid, B., and Matthews, A.: Vertical variations of cloud microphysical relationships in marine stratocumulus clouds observed during the ACE-ENA campaign, J. Geophys. Res. Atmos., 126, e2021JD034700, https://doi.org/10.1029/2021JD034700, 2021.

Yeom, J. M., Szodry, K., Siebert, H., Ehrlich, A., Mellado, J. P., Shaw, R. A., and Yum, S. S.: High-resolution measurements of microphysics and entrainment in marine stratocumulus clouds, Q. J. R. Meteorol. Soc., 150, 81–97, https://doi.org/10.1002/qj.4586, 2024.

Yin, B. and Albrecht, B. A.: Spatial variability of atmospheric boundary layer structure over the eastern equatorial Pacific, J. Climate, 13, 1574–1592, https://doi.org/10.1175/1520-0442(2000)013<1574:SVOABL>2.0.CO;2, 2000.

https://doi.org/10.5194/egusphere-2026-3376
Preprint. Discussion started: 6 July 2026

Zhang, H., Zheng, Y., and Li, Z.: Influence of Surface Aerosol Injection on Stratocumulus-to-Cumulus Transition: Cloud-Surface Coupling and Background Aerosol Concentrations, J. Geophys. Res. Atmos., 131, e2025JD044444, https://doi.org/10.1029/2025JD044444, 2026.

Zheng, Y., Rosenfeld, D., and Li, Z.: Estimating the Decoupling Degree of Subtropical Marine Stratocumulus Decks From Satellite, Geophys. Res. Lett., 45, https://doi.org/10.1029/2018GL078382, 2018a.

Zheng, Y., Rosenfeld, D., and Li, Z.: The relationships between cloud-top radiative cooling rates, surface latent heat fluxes, and cloud-base heights in marine stratocumulus, J. Geophys. Res. Atmos., 123, https://doi.org/10.1029/2018JD028579, 2018b.